UCLouvain

École polytechnique de Louvain

# Numerical study of particle harvesting in micro-channels

Author: **Clément DE SCHAETZEN**
Supervisor: **Pr. Miltiadis PAPALEXANDRIS**
Readers: **Pr. Juray DE WILDE, Dr. Christos VARSAKELIS**
Academic year 2019–2020
Master [120] in Mechanical Engineering

**Abstract**

In this master thesis, we are completing a numerical study of the Poiseuille flow of dense non-colloidal mono-disperse suspensions in micro-channels at low-Reynolds number. The end goal is to estimate the feasibility of a passive and continuous particle harvesting system taking advantage of the shear induced particle migration phenomenon.

The first part is dedicated to a literature review where we are describing the characteristics of dense suspensions and the different theoretical models used to describe the tendency of particles to migrate to the center of the channel.

Then, we develop the governing equations used to model the behaviour of the suspensions taking for hypotheses that the solutions are time independent and that the variables are uni-directional. These equations are based on a recently developed two-phases model. The migration of the granular phase is based on a advection-diffusion model in the form a compaction equation that evaluates the granular pressure with the intergranular stresses and a diffusion term.

Finally, we present and discuss the different obtained numerical results. First, we study horizontal channels where the suspension is driven by a pressure gradient. Secondly, we compare these results with gravity driven flows in vertical channels in order to evaluate the performance of a passive particle harvesting system. The parameters we analyse are the average particle volume fraction, the channel height and the velocity reached at the center. Then, we analyse how modifying these impact the mass-flow of collected particles with the help of mass-flow coefficients. We also analyse the impact of the used draw law, the domain size and the boundary conditions. The last section is a comparison with dry granular media.

**Acknowledgements**

I am very grateful for my thesis supervisor Pr. Miltiadis Papalexandris for its always responsive attention and his wise advice.

I would like to thank Dr. Christos Varsakelis for having clarified the objectives of this thesis. I would also like to thank him together with Pr. Juray de Wilde for his participation in the evaluation of this work as readers.

I am also appreciative of Anouk Riffard and Constantin Sula who helped in the technical set up at the start of my thesis.

Finally, I would like to thank my family and friends that supported me, not only for this final year but throughout this exciting journey at UCLouvain.

# Contents

# Nomenclature

| | |
|---|---|
| $\phi_f$ | Volume fraction of the fluid phase |
| $\phi_s$ | Volume fraction of the granular phase |
| $\bar{\phi}_s$ | Average volume fraction of the granular phase |
| $\beta_s$ | Inter-granular stress [Pa] |
| $\beta_w$ | Parameter to match experimental data in slip law |
| $\delta$ | Drag coefficient $[\frac{Pas}{m^2}]$ |
| $\delta_{slip}$ | Thickness of the slip layer [m] |
| $\dot{\gamma}$ | Local shear rate [1/s] |
| $\gamma_s$ | Coefficient involved in the stresses that are developed due to rearrangements of the interfacial aera density [N] |
| $\mu_f$ | Viscosity of the fluid phase [Pa s] |
| $\mu_s$ | Normal stress viscosity [Pa s] |
| $\mu_{susp}$ | Viscosity of the suspension [Pa s] |
| $\phi_s$ | Volume fraction of the granular phase |

$\phi_{jam}$ Volume fraction of the granular phase at jamming transition

$\rho_f$ Density of the granular phase $[\frac{kg}{m^3}]$

$\rho_s$ Density of the solid phase $[\frac{kg}{m^3}]$

$\rho_{susp}$ Averaged density of the suspension $[\frac{kg}{m^3}]$

$\tau_f$ Viscous stress tensor of the fluid phase

$\tau_s$ Viscous stress tensor of the granular phase

$\tau_w$ Viscous stress at the wall [Pa]

$\mathbf{V}$ Strain of rate tensor $[\frac{1}{s}]$

$\mathbf{V}^d$ Deviatoric part of the strain of rate tensor $[\frac{1}{s}]$

$\mathbf{V}^s$ Statoric part of the strain of rate tensor $[\frac{1}{s}]$

$\zeta_f$ Bulk viscosity of the fluid phase

$\zeta_s$ Bulk viscosity of the granular phase

$p_f$ Fluid pressure [Pa]

$p_s$ Granular pressure [Pa]

$Re_p$ Particle Reynolds number $= \frac{\rho_f u_{slip} D}{\mu_f}$

$u_f$ Velocity of the fluid phase [m/s]

$u_s$ Velocity of the granular phase [m/s]

$u_w$ Velocity f the wall (null in our case) [m/s]

$u_{max}$ Center-line velocity in a single phase Poiseuille flow [m/s]

$u_{slip}$ Slip velocity $=|u_f - u_s|$ [m/s]

$u_{susp}$ Averaged velocity of the suspension [m/s]

D Diameter of the particles [m]

| | |
|---|---|
| $D_B$ | Diffusivity constant $[\frac{m^2}{s}]$ |
| F | Pressure gradient driving the flow $[\frac{Pa}{m}]$ |
| g | Gravity $[\frac{m}{s^2}]$ |
| J | Diffusive flux of particles $[\frac{1}{s}]$ |
| k | Boltzmann constant $[\frac{J}{K}]$ |
| Pe | Peclet number of the flow $= \frac{\dot{\gamma}D^2}{D_B}$ |
| Re | Reynolds number of the flow $= \frac{\rho_f u_c l_{ref}}{\mu_f}$ |

# 1 Introduction

Filtration and particle harvesting is a ubiquitous and crucial step for biochemical, pharmaceutical and environmental applications. Research on this topic has gained momentum thanks to the use of micro-fluidic applications. Different micro-fluidic devices are already available for separating cells, handling blood or suspensions of DNA but are limited to small scale applications. [8] The goal of this master thesis is to study the feasibility of micro-fluidic devices taking advantage of the shear induced particle migration in micro-channels.

Micro-channels can be defined as channels whose dimensions are less than 1 millimetre and greater than 1 micron. They can be fabricated in many materials; glass, silicon, polymers and even metal. The primary advantage of micro-scale devices is the good match with the scale of biological structures and the potential for placing multiple functions for chemical analysis on small area. [42] This is the reason why in the 1990s, the Defense Advanced Research Projects Agency of the US Department of Defense supported a series of programmes aimed at developing field-deployable micro-fluidic systems designed to serve as detectors for chemical and biological threats (military and terrorist), that where increasing after the cold war. These programmes were the main stimulus for the rapid growth of academic micro-fluidic technology. [47] The micro-channels also offer the advantage of exhibiting high shear rates while remaining at low Reynolds number.

The idea is to replace the previously used membrane micro-filtration because they suffer from the issue of membrane clogging. [45] This phenomenon significantly limits the efficiency and the reliability of the filtration process since the majority

of the operations costs of this kind of filtration is consumed by the replacement of the membrane filter. This is the reason why continuous filtration systems are preferred.

The passive techniques include hydrophoresis [3], deterministic lateral displacement [28] and gravitational methods [15]. The two first are based upon the fluid and particles interacting with structures along the channel to cause the separation of particles by size. They benefit from being continuous and passive but the manufacture of these obstacles can become complex. The working principle of the gravitational method is to use the fact that different size particles will have different terminal velocities in a gravitational field. This is because buoyancy force and Stokes drag scale with volume and diameter respectively.
The active methods are using an externally applied force field in order to induce fractionation. We can cite several different methods; dielectrophoresis [24], acoustophoresis [38] and magnetophoresis [32]. These are all considered FFF techniques (field flow fractionation) in the sense that the particles within a flow are moving at relatively uniform velocities and then a certain type of field is applied causing the separation of the particles by size or properties.
Current research is also led on inertial focusing method [31]. Reliance on the inertia of the fluid in the system rather than on limiting its effects, as is normally done in micro-fluidics, can result in a significantly higher throughput.

In this master thesis, we will focus on the shear induced particle migration. Indeed, it has been observed since 1966 in pipe Poiseuille flows [20] and 1994 in channel confined flows [22], that due to inter-particles collisions, particles tend to migrate from high shear rate zones to the lower shear rate zones; the center of the channel and form a central-plug zone. This observed peak of particles is not sharp but fairly smooth. The idea is to separate the fully developed flow in three different channels; a top, center and bottom channels. The center channel thanks to particle migration will then be more concentrated in particles than the top and bottom channels. Taking advantage of this physical phenomenon would induce a gain in cost and time efficiency since the filtration will become a continuous, non invasive and passive process.

# 2 Literature Review

## 2.1 Dense Suspension: Physical understanding

Granular suspensions are composed of a mixture of particles suspended in a fluid phase. This thesis is dedicated to non-colloidal suspensions, in the sense that the brownian motion of the particles can be neglected. The radius of the particles in these suspensions is thus in the range of 1 $\mu$m and 100 $\mu m$ for the thermal fluctuations to be neglected, while the colloidal suspensions are composed of smaller particles (up to the nanometer).

Flows of granular suspensions are omnipresent in biological systems (blood), natural phenomena (mud, sediment transport, submarine avalanches,...) and industrial processes; from cosmetics, food, civil engineering materials, pharmaceutical products, to the paper and petroleum industry. The fact that we encounter granular suspensions in so many phenomena and the complexity of these flows explains the several years of study and the growing number of publications on the subject.

Dense or highly concentrated suspension can be defined as a suspension where the average separation distance between the particles is equal to or smaller than the particle size. The rheology is non-Newtonian and multiple body interactions and lubrication forces both significantly contribute to the rheology.

The goal is to establish constitutive laws for this rheology. But we will see in the rest of this thesis that the challenge with dense suspensions is that there is not scale segregation. Mesoscopic phenomena such as inter-particle interactions and particle rearrangements have an influence on the bulk properties.

### 2.1.1 The suspension as an effective fluid

History of the study of suspensions begins with Einstein in 1906.[30] He studied the increase of viscosity of a viscous Newtonian fluid when adding a few particles. This is called the dilute regime. His idea was to study a suspension as an effective fluid. In 1911, he established a linear correlation linking the viscosity of the suspension $\mu_{susp}$ to the volume fraction of non-deforming particles $\phi_s$.

$$\tilde{\mu}_{susp} = \frac{\mu_{susp}}{\mu_f} = 1 + \frac{5\phi_s}{2} \tag{2.1}$$

where n is the sphere number density and the volume fraction $\phi_s$ is defined as:

$$\phi_s = \frac{4}{3} n\pi D^3 \tag{2.2}$$

We can notice that the tilde is a notation to express the non-dimensionalisation of the viscosity of the suspension by the viscosity of the fluid. This convention will be used for the rest of the document, where the non-dimensionalisation will be done with respect to the fluid properties.
This increase of viscosity can be explained by the disturbance induced by the particle to the fluid. The non-buoyant sphere (with the same density as the fluid) is freely suspended in the shearing flow and thus experiences no hydrodynamic force or torque. The particle, experiencing shear from the flow, can freely rotate but resists the straining component of the shearing flow. This resistance leads to an increase of the energy dissipation and thus an increase in viscosity of the suspension.

### 2.1.2 Stokesian dynamics

Then in the 1960's-1970's, researchers focused on more concentrated suspensions, the semi-dilute regime. In this regime, hydrodynamic forces or lubrification forces come into play. We are in the Stokes flow regime, where inertial forces are neglected and the Reynolds number is thus vanishingly small. (Re « 1) We can then linearise Navier-Stokes equations since the viscous effects are dominant compared to inertia. The shear stress $\tau$ scale linearly with the shear rate $\dot{\gamma}$. The viscosity

of the suspension $\mu_{susp}$ is thus a sole function of the volume fraction $\phi_s$. Hence, the suspension in semi-dilute can be seen as a Newtonian fluid with a viscosity increasing with $\phi_s$. This velocity is not increasing linearly as Einstein supposed but diverges when $\phi_s$ approaches $\phi_{jam}$. Several correlations exists and are represented on fig 2.1. The most popular correlation known as Krieger's correlation.[25]

$$\tilde{\mu}_{susp} = \left(1 - \frac{\phi_s}{\phi_{jam}}\right)^{-2.5\phi_{jam}} \tag{2.3}$$

This correlation is coherent with reality since the viscosity diverges at $\phi_s = \phi_{jam}$, where the suspension ceases to flow. This jamming transition happens close to the maximum packing fraction. In this document, we will fix $\phi_{jam} = 0.6$. We can see that Einstein linear correlation is valid and coherent with the other correlation for low volume fraction, below 0.1.

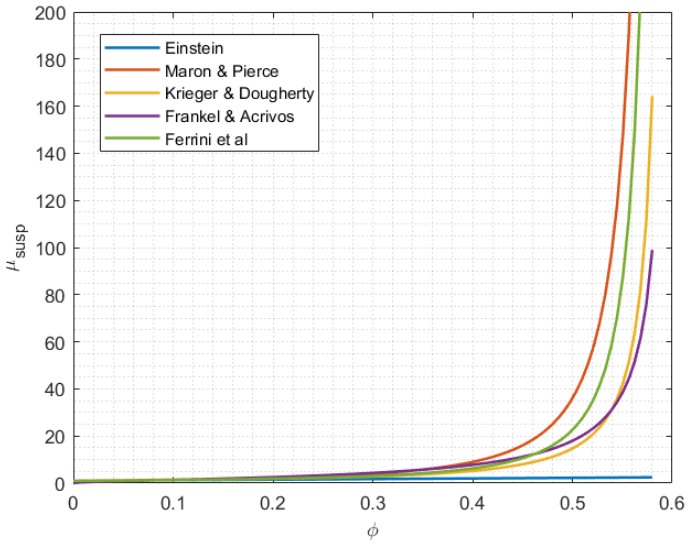


Figure 2.1: Relative viscosity in function of the volume fraction, with Einstein's (dilute hard-spheres suspensions), Krieger–Dougherty's correlation (semi-dilute) and other correlations

## 2.2 Mesoscopic phenomena

The dilute and semi-dilute regimes are well understood since the pioneering work of Einstein. The study of the past 30 years is focused on dense regime where the average distance between particles is smaller than the particle size. [44] Describing a suspension as an effective fluid does not take into account mesoscopic phenomena, phenomena manifesting themselves at the particle scale. Indeed, there exist several mechanisms (inter-particle interaction, particle rearrangement) that can lead to a non uniformity of the volume fraction in the flow even in the regions away from the boundary. When this occurs, macroscopic measurements such as viscosity will exhibit non Newtonian behaviour. Plenty of efforts has been developed in order to establish constitutive laws taking into account these non-Newtonian behaviours. In this section, we will cover the different mechanisms and we will especially focus on shear induced particle migration. We will see the different used models describing this migration and analyse how they compare to each other. We insist that in these systems, the forces in play between non-colloidal particles are a combination of hydrodynamic and contact forces. [2]
The main mechanism is the lateral migration (along y in our frame of reference) that produces cross-stream irreversible motions of particles. Among these, we have: the inertia-driven migration (responsible for the Segré-Silberberg effect [40]), migration due to the deformability of the particles leading to a clear fluid near the walls in a blood flow (Fahraeus-Lindquist [7]) or even migration due to non-Newtonian properties of the suspending fluid. The inertia driven migration or inertial lift is also known as the turbulent diffusion. It is dominant when $Re_p$ is high. It is also studied for continuous filtration method in curving micro-channels. [4]
In this master thesis, we are staying in a low range of $Re_p$ and we are thus focusing on shear-induced particle migration.

## 2.3 Shear-induced particle migration

As mentioned in the introduction, shear induced particle migration has been observed since the 1960's. It is the tendency of particles to migrate from the high shear rate zones to the low shear rate zones. In the case of Poiseuille flow, the

particles have thus the tendency to migrate irreversibly to the center of the channel. This phenomena is not due to inertia since the Stokesian dynamics impose a zero Reynolds number. This phenomenon was first described by Eckstein et al. in 1977 [5], who stated that when a relatively dense suspension is subjected to shear, inter-particle collisions give rise to migration away from the average streamlines. When two particles interact, they just continue in their respective flow lanes after passing around each other. However, when the volume fraction is high enough for multiple particles to interact, a net lateral displacement occurs.[21]
This mechanism is in competition with Brownian motion (random movement of particles in a fluid) that are restoring the uniformity of the volume fraction. The balance between the two mechanisms is determined by the Péclet number, where $D_B$ is the diffusivity constant.

$$Pe = \frac{\dot{\gamma} D^2}{D_B} \tag{2.4}$$

$$D_B = \frac{kT}{6\pi\mu_f D} \tag{2.5}$$

Nevertheless, when the size of particles is between 1 and 100 microns, the inter-particle interaction is dominant over Brownian diffusion. We are thus in the high Péclet number limit. We will now analyse the main models used in the literature.

### 2.3.1 Diffusion model

The first explicitly recognition of the migration due solely to irreversible particles interaction is attributed to Leighton & Acrivos in 1987 [27]. By using scaling arguments, the authors were able to derive a general expression for the diffusive flux of the particles in a shearing flow, expressed in terms of the gradients of the particle concentration and shear rate. Viscosity gradients are also important and particle migration upon collision takes place in a the direction of a diminishing viscosity.[39] The expression reads:

$$\frac{d\phi_s}{dt} + u \cdot \nabla\phi_s = -\nabla \cdot J \tag{2.6}$$

$$J = -K_c D^2(\phi_s^2 \nabla\dot{\gamma} + \phi_s \dot{\gamma} \nabla\phi_s) - K_{\mu_{susp}} \dot{\gamma} \phi_s^2 \left(\frac{D^2}{\mu_{susp}}\right) \frac{d\mu_{susp}}{d\phi_s} \nabla\phi_s \tag{2.7}$$

where $K_c$ and $K_{\mu_{susp}}$ are constants to be determined empirically. The rest of the symbols are defined in the nomenclature as they appear in the rest of the document. We notice in this equation that the diffusive flux J is always proportional to the shear rate. When $\dot{\gamma}$ is null, the flux J is null too. This model does not incorporate resisting mechanism to the particle migration in low shear rate regions, the center of the channel.

### 2.3.2 Suspension balance model

A more recent and rather successful model, developed by Nott and Brady in 1994 [36] and Morris and Boulay in 1999 [35], called the suspension balance model, relates the particle migration flux to the divergence of the normal stresses of the particle phase. This model assigns each phase its momentum equation and introduces the normal stresses as a rheological property of the suspension. This model is in good agreement for suspensions flows in the Stokes approximation. [39] But it does not take into account inertial effect which can cause issues with flows with buoyant particles ($\rho_s$ not equals to $\rho_f$).

$$\frac{d\phi_s}{dt} + u \cdot \nabla\phi_s = -\frac{D^2}{18} Re \nabla(f(\phi_s))\nabla \cdot \tau) \tag{2.8}$$

where f($\phi_s$) is called *sedimentation hindrance function* [35] and $\tau$ is the viscous stresses tensor of the granular phase. The next section is dedicated to the derivation of this viscous stresses tensor.

#### Viscous stresses

To define a Newtonian fluid, there are two variables needed, the shear viscosity $\mu_f$ and the bulk or volume viscosity $\zeta_f$, also known as the second coefficient of viscosity. They are needed to define the viscous stress tensor $\tau$. This tensor is derived from splitting the rate of strain tensor $\mathbf{V}$ in a deviatoric and spherical part, the first representing pure volumetric rate of deformation and the second pure shear rate of deformation. The spherical part $\mathbf{V}^s$ (compression/extension, no shear) is proportional to the sum of the diagonal element of $\mathbf{V}$ (the trace of $\mathbf{V}$), while the deviatoric part $\mathbf{V}^d$ is found with a difference of the total rate of strain

tensor $\mathbf{V}$ and $\mathbf{V}^s$.[12]

$$\mathbf{V} = -\frac{1}{2}\left(\nabla u + \nabla u^T\right) = \mathbf{V}^d + \mathbf{V}^s \tag{2.9}$$

$$\mathbf{V}^s = -\frac{1}{3} trac(\mathbf{V}) I = -\frac{1}{3}\nabla \cdot uI \tag{2.10}$$

$$\mathbf{V}^d = \mathbf{V} - \mathbf{V}^s = \mathbf{V} + \frac{1}{3}\nabla \cdot uI \tag{2.11}$$

Then, the two effects of the rate of strain are summed, each one of them weighted by their two respective viscosities $\mu_f$ and $\zeta_f$:

$$\tau = 3\zeta_f \mathbf{V}^s + 2\mu_f \mathbf{V}^d = -\zeta_f \nabla \cdot uI + 2\mu_f \left(\mathbf{V} + \frac{1}{3}\nabla \cdot uI\right) \tag{2.12}$$

$$\tau = -\left(\zeta_f - \frac{2}{3}\mu_f\right)\nabla \cdot uI + 2\mu_f \mathbf{V} \tag{2.13}$$

We notice that in equ. 2.13, if we are in a case of a single phase incompressible flow, $\rho_f$ is constant, this leads to $\nabla \cdot u = 0$ by continuity. The first term of the equation is thus null and the bulk viscosity is superfluous. We then arrive on Newton's law of viscosity (in 3D) that is linking linearly the viscous stresses to the strain rate tensor with a proportional constant, the shear viscosity $\mu_f$.

$$\tau = 2\mu_f \mathbf{V} = -\mu_f(\nabla u_f + \nabla u_f^T) \tag{2.14}$$

Newton's law converts in 2D with unidirectional velocity to:

$$\tau = -\mu_f \frac{du_f}{dy} \tag{2.15}$$

This law of viscosity is sufficient to derive the viscous stress tensor in applications where the volume viscosity $\zeta_s$ is zero (mono-atomic gas at low density) or incompressible flows as just demonstrated. However, the bulk viscosity is important in our case since the term $\nabla \cdot u$ is non-null due to the effect of the granular phase.

The viscous stress tensors of the fluid and granular phase $\tau_f$ and $\tau_s$ are then

given by:

$$\tau_f = -\zeta_f \nabla \cdot u_f \mathbf{I} + 2\mu_f \mathbf{V}_f^d \tag{2.16}$$

$$\tau_s = -\zeta_s \nabla \cdot u_s \mathbf{I} + 2\mu_s \mathbf{V}_s^d + \chi_a \mathbf{I} + \chi_b \mathbf{V}_s \cdot \mathbf{V}_s \tag{2.17}$$

where $\chi_a$ and $\chi_b$ are terms added for granular viscous stresses. The interested reader is redirected to the appendix where further developments are made. We are developing the initial governing equations, using these definitions of the viscous stresses, which are valid for general cases and deriving the governing equations in our case (uni-dimensional, steady-state).
In [35], in order to provide insight of the influence of normal viscous stresses on the suspension behaviour while keeping the model sufficiently simple to allow for steady-state predictions, they model the granular viscous stresses $\tau_s$ with the help of two viscosities, the shear viscosity and the *normal stress viscosity* $\mu_n$.

$$\tau_s = -\mu_n \sqrt{2\mathbf{V}_s : \mathbf{V}_s}\mathbf{Q} + 2\mu_s \mathbf{V}_s \tag{2.18}$$

where

- $\mu_n$ is defined as the normal stress viscosity, which expresses the capacity of granular media to support normal viscous stresses due to shear deformation.
- $\sqrt{2\mathbf{V}_s : \mathbf{V}_s}$ is the local shear rate, $\dot{\gamma}$
- Q is the tensor that accounts for anisotropy of the normal viscous stresses.

$$Q = \begin{pmatrix} 1 & 0 & 0 \\ 0 & \lambda_2 & 0 \\ 0 & 0 & \lambda_3 \end{pmatrix} \tag{2.19}$$

- $\mu_s$ is the apparent shear viscosity of the granular phase

The derivation of $\mu_s$ and $\mu_n$ is made in the section dedicated to material parameters and derived from Morris and Boulay [35]. (4.1.2) They are both depending on the volume fraction $\phi_s$.

### Normal stress differences

To identify and distinguish different non-Newtonian flows, we need coefficients called normal stress differences $N_1$ and $N_2$ that describe the anisotropy of the viscous stresses.[41, 13]

$$N_1 = \Sigma_{22} - \Sigma_{11} \tag{2.20}$$

$$N_2 = \Sigma_{22} - \Sigma_{33} \tag{2.21}$$

In the case of dense suspension, normal stresses differences are appearing. They are seen to strongly increase for a volume fraction above 0.22. The negative contribution to $N_1$ is due to the synergic action of hydrodynamic and contact forces between the suspending particles.[41] By contrast with the positive $N_1$ measured for visco-elastic fluids, negative values of $N_1$ are considered an unusual and unique rheological feature of suspensions. In their article from 1999, Morris & Boulay estimate the values of $\lambda_2$ and $\lambda_3$ to 0.8 and 0.5 respectively in order to match with their experimental measurements. These have been fixed at $\lambda_2 \approx 0.95$ and $\lambda_3 \approx 0.6$ by Boyer et al. [2]

# 3

# Governing Equations

In this chapter, we will go through the different equations that govern the flow of suspensions. Fully developed flows at low Reynolds number have served as the primary test case in several studies due to their easy reproductibility. There is a good collection of experimental data to compare the results of the models with. Nonetheless, despite their conceptual simplicity, they exhibit complex features that is typical of suspensions flows. [34]
In this study, we focus on unidirectional, steady and at first with constant density flows. In the first part, we will study horizontal channels where the flows will be pressure driven. In this case, since we are studying small channel sizes and high particle concentrations, the lateral effect of gravity is expected to be small. For this reason, gravity does not appear in the momentum balances along y. (Equ 3.6 & 3.8)
Afterwards, we will study gravity driven flows, in vertical channels. The pressure gradient, acting as forcing term, will be replaced by a gravity term containing the density of the two phases.

## 3.1 Single phase Poiseuille flows

First, we analyse the single-phase Poiseuille flow. The flow of the fluid phase will help us to compare with the suspension flows. For example, we will use the center-line velocity of the single phase flow as the maximum velocity for the non-dimensionalisation.
Poiseuille flow is defined as a fully developed flow (flow where the velocity does not

change along x) in a channel or pipe with constant area.

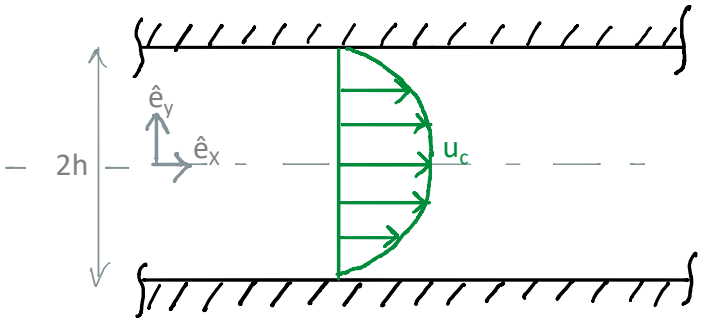


Figure 3.1: Single phase flow

In a channel, Navier-Stokes equation for the momentum of the single phase flow reduces to:

$$\frac{dp}{dx} = F = \mu_f \frac{d^2u}{dy^2} \tag{3.1}$$

The pressure gradient is overcoming the viscous dissipations in order to drive the flow. It will be defined as F, in the rest of this document, to remain coherent with [34]. By integrating twice along y, we have:

$$u(y) = F\mu_f \left( \frac{y^2}{2} + C_1 y + C_2 \right) \tag{3.2}$$

The fluid sticks to the wall, the velocity at $y = -h$ and $y = h$ is thus equal to 0.

$$u(y) = -F\frac{h^2}{2\mu_f} \left( 1 - \left( \frac{y}{h} \right)^2 \right) \tag{3.3}$$

The velocity profile is parabolic. The maximal velocity, the center-line velocity $u_c$, is equal to:

$$u_c = -F\frac{h^2}{2\mu_f} \tag{3.4}$$

## 3.2 Pressure driven two phase flows

In this thesis, we study the behaviour of dense suspensions. There is thus a volume fraction of particles (non deformable spheres of a diameter between 1 $\mu m$ and 100 $\mu m$) between $\phi_s = 0.3$ and $\phi_{jam}$. The particularity of our model is to consider the two phases and consider the momentum exchange between the two with a drag law. We then have four different equations. The development comes from [34] and the non dimensionalisation is written in the appendix for the interested reader.

### 3.2.1 Reference values

The fluid is a mix of water and glycerin and the granular phase is made of silica particles. We use the fluid's values as reference values:

- $\rho_{ref} = \rho_f = 10^3 kg/m^3$
- $\mu_{ref} = \mu_f = 4e^{-2} Pa \cdot s$
- $l_{ref}$, the channel's half width
- $u_{ref} = u_c$, the center-line velocity of the equivalent single phase flow.
  The center-line velocity of a single phase gravity driven Poiseuille flow is equal to:
  $$u_{ref} = u_c = -F \cdot \frac{l_{ref}^2}{2\mu_f} [m/s]$$
- $g = 9,81 m/s^2$
- $Re = \frac{\rho_{ref} u_{ref} l_{ref}}{\mu_{ref}}$

## 3.3 Governing equations

The equations are based on a two-phase continuum model. Different hypotheses are applied. We are studying a steady state flow. Indeed, it is preferred in the industry to have flows whose characteristics are constant with time. We assume that the velocities are unidirectional, they only depends on y, the wall coordinate, and aligned along x, the streamwise direction. We stress that we are in a low Reynolds number limit, the flow thus always remains laminar.
We first use the conservation of momentum of the fluid and granular phase to obtain the three first equations. The two first are very similar and describe the conservation of momentum along x for each phase. We can see that the forcing term F is inducing an increase of the fluid and granular velocities respectively. The drag term $\delta$ is the *Robin Hood* term. It is balancing the two velocities in order to make them equal. For example, in 4.5, when $u_f$ is bigger than $u_s$, this term will be positive and will then counteract F (which is negative). The increase of $u_f$ will then be smaller if $u_f$ is bigger than $u_s$. The opposite is true as well. The drag induces a momentum exchange between the two phases in order to induce a velocity equilibration during the development of the flow. The integration of the momentum equation of the fluid phase along y yields that the fluid pressure $p_f$ is constant. Without loss of generality, it can be set to $p_f = 0$. Note that it is because gravity can be neglected in this case. Otherwise, $p_f$ would not be constant. We will assume that the suspension is saturated.

$$\phi_s + \phi_f = 1 \tag{3.5}$$

**Fluid phase**

$$\frac{1}{Re}\frac{d}{dy}\left((1-\phi_s)\frac{d\tilde{u_f}(y)}{dy}\right) = \tilde{\delta}(\tilde{u_f} - \tilde{u_s}) - \tilde{F}(1-\phi_s) \tag{3.6}$$

**Granular phase**

*along x:*

$$\frac{1}{Re}\frac{d}{dy}\left(\tilde{\mu}_s\phi_s\frac{d\tilde{u_s}(y)}{dy}\right) = -\tilde{\delta}(\tilde{u_f} - \tilde{u_s}) - \tilde{F}(\phi_s) \tag{3.7}$$

We can notice that if we set $\phi_s = 0$ for the two first equations, since the drag term will be null, the equ. 3.7 will become $0 = 0$ and the equ. 3.1 will become, as expected, the same as the single phase equation.

*along y:*

$$\frac{1}{Re}\frac{d}{dy}\left(\tilde{\mu_n}\phi_s|\frac{d\tilde{u_s}(y)}{dy}|\right) = -\frac{d}{dy}\left(\gamma_s\left(\frac{d\phi_s}{dy}\right)^2\right) - \frac{d}{dy}(p_s\phi_s) \tag{3.8}$$

The third equation, which is describing the conservation of momentum in the granular phase along y is of primary importance to understand the particle migration. It contains three terms; the normal viscous stresses, the non local stresses and the pressure term. The viscous term is the same as in 4.6 except from the shear viscosity which is replaced by the *normal stress viscosity*. The normal viscous stresses are pushing the particles from higher shear rate zones to low shear rate zones, from the wall to the center of the channel. The non-local stresses and the pressure term are counter-acting these viscous stresses. The non-local stresses, depending on the size of the particles are developed due to variations in the contact between grains. The pressure term describes the pressure in the granular phase and it is obtained thanks to the last equation; the compaction equation. An analysis of the variation of these stresses along the channel height will be described in the results.

**Compaction equation**

$$p_s - \beta_s + \frac{d}{dy}\left(\gamma_s\frac{d}{dy}\phi_s\right) = 0 \tag{3.9}$$

This equation establishes the particle pressure thanks to the intergranular stress $\beta_s$ and the value $\gamma_s$. These are both thermodynamic derivatives depending on the micro-structure of the granular phase. $\gamma_s$ is defined as the derivative of the Helmotz free energy of the granular phase with respect to $\nabla\phi_s$. $\beta_s$ is the derivative of the Helmotz free energy of the granular phase with respect to $\phi_s$ and is also referred as configuration pressure. The term $\beta_s$ is generally called intergranular stresses while the term containing $\gamma_s$ is known as the diffusion term. These two mechanisms are then in competition with each other in order to increase $p_s$, since $\beta_s$ is positive and increases with $\phi_s$ and $\gamma_s$ is negative and increases also with $\phi_s$. The particularity

is that the intergranular pressure increases with $\phi_s$ while the diffusion increases quadratically with the gradient of $\phi_s$. In the section dedicated to the results, we will analyse the balance between these two terms in different cases.

## 3.4 Comparison of the advection-diffusion model with other models

The model used in the numerical algorithm is based on an advection diffusion model with a two phases continuum. It presents different advantages compared to the two models presented in the literature review.

Firstly, compared to the diffusion model, the compaction equation does not include the shear rate $\dot{\gamma}$, while it appears in all the terms of 3.5. Consequently, the diffusion model does not make intervene any resisting terms to the particle migration at the center; while it is observed that for low volume fraction the peak at the center is bounded below $\phi_{jam}$.

The used model is closer to the suspension balance model that also use a two phase continuum model, with a momentum exchange between the two phases. The two models describe migration with stresses acting on the granular phase. The difference lies with the fact that we use a pressure difference $p_s - p_f$ while the suspension balance model sticks with a divergence of the viscous stress tensor. They also need the suspension velocity, which is not needed in the advection-diffusion model. In the suspension balance model, to avoid the prediction of cusps at zero shear rate (as it is the case for the diffusion model), they are using an ad-hoc term linked to the particle diameter. This method is similar to what is done with $\gamma_s$ that appears in the diffusion term.

# 4 Numerical Model

## 4.1 Material parameters

In order to close the equations, we need to use correlations estimating the material parameters; the transport coefficients; $\mu_s$, $\mu_n$ and $\delta$ and the thermodynamic derivatives; $\beta_s$ and $\gamma_s$. We will remain with the same correlations used in [34]. As regards $\beta_s$ and $\gamma_s$, since they are thermodynamic derivatives, they have to be derived via experimental measurements.

### 4.1.1 Drag law

For the drag law, an extension of the Hill-Koch-Ladd drag correlation is used. This correlation has been established in order to widen the range of validity of volume fractions and particle Reynolds numbers. It has the particularity of estabilishing a continuous evolution of the drag coefficient with respect to the particle Reynolds number. Indeed, between values of $Re_p$ from 1 to 10, there were discontinuties that have been smoothed, as seen on fig. 4.1. The correlation is based on data from Lattice–Boltzmann simulations (DNS) [1]. In this law, $\delta$ is depending on the particle diameter D, $\mu_f$, $\phi_s$, the drag coefficient $C_d$ and $Re_p$ which is defined with respect to the slip velocity $u_{slip} = |u_s - u_f|$.

$$\delta = \frac{3}{4}\frac{C_d(1-\phi_s)\rho_f\phi_s|u_s-u_f|}{D} = \frac{3}{4}\frac{\mu_f\phi_s C_d Re_p}{D^2} \tag{4.1}$$

In the case of our study, the suspension is dense and the particles are very small (D= $1\mu m$). This then leads to high interphasial drag and thus a constant velocity equilibration. The value of the particle Reynolds is very low ($Re_p << 1$), we are then in the range where the drag coefficient is proportional to the inverse of the Reynolds number, as seen on fig 4.1.

$$C_d \propto \frac{f(\phi_s)}{Re_p} \tag{4.2}$$

In the case where $\phi_s$ is 0.1%, we are in the Stokes regime and we know the relation:

$$C_d = \frac{12}{Re_p} \tag{4.3}$$

In the article, they find the relation of $C_d$.

$$C_d = \frac{12(1-\phi_s)^2 f}{Re_p} \tag{4.4}$$

where f is the expression calculated in the correlation in function of the different intervals of $\phi_s$ and Re.

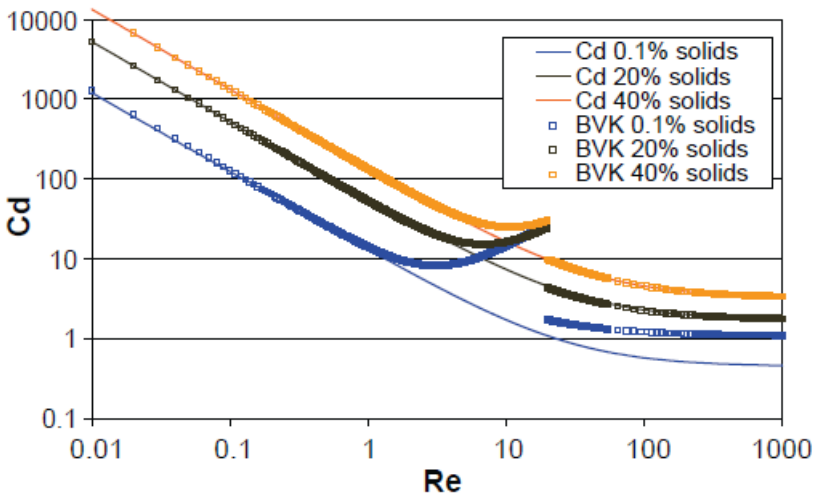


Figure 4.1: Drag coefficient variation in function of the particle Reynolds number, taken from [1], similar to Moody's diagram

In the range of dense suspension ($\phi_s$ between 0.3 and $\phi_{jam}$), f is depending quadratically on the particle Reynolds number.

$$f = f_0 + f_1 Re_p^2 \tag{4.5}$$

For further information on the values of $f_0, f_1$ or $f_2, f_3$ for higher $Re_p$, we redirect the reader to [1]. The value of $\delta$ is then estimated, solely with $\phi_s$, f, $\mu_f$ and D:

$$\delta = 18\mu_f(1-\phi_s)^2\phi_s\frac{f}{D^2} \tag{4.6}$$

### 4.1.2 Transport coefficients

For the coefficients used for the viscous stresses, the correlation is based on the work from [35], where the two viscosities are non dimensionalised with respect to the carrier fluid's viscosity $\mu_f$.

$$\tilde{\mu}_s = \frac{2.5}{\phi_{jam}-\phi_s} + 0.1\frac{\phi_s}{(\phi_{jam}-\phi_s)^2} \tag{4.7}$$

Normal stress differences are known to follow forms similar to the viscosity model. The basic argument supporting the similarity of the various viscometric functions is that all stresses in the dense limit are due to similar shear-driven mechanisms, namely, moments of the lubrication and contact stress.[35, 37]

$$\tilde{\mu}_n = 0.75\frac{\phi_s}{(\phi_{jam}-\phi_s)^2} \tag{4.8}$$

### 4.1.3 Intergranular stresses $\beta_s$

The intergranular stresses are known to increase with the volume fraction, vanishing for small values of $\phi_s$ and diverging at $\phi_{jam}$. As the particles accumulate, they are compacted. As it approaches $\phi_{jam}$, where the particles do not flow anymore, these intergranular stresses increase drastically. The grains are resisting the compaction. A simple law is derived from a logarithmic relation:

$$\beta_s = -\beta_0 log(\phi_{jam}-\phi_s) \tag{4.9}$$

### 4.1.4 $\gamma_s$

They are only a few experimental measurements for $\gamma_s$, a simple power law is thus established here but a linear law could have been considered as well. It is expected to vanish at zero volume fraction, since it is also related to the microstructure. In other studies, diverging expressions also have been used. The behaviour of $\gamma_s$ still being unknown close to the jamming transition, we prefer to remain with a power law. The factor r can be arbitrarily chosen. In this case, a factor r equals to 6 appears to give numerical results closer to experimental measurements.

$$\gamma_s = -\gamma_0 \phi_s^r \tag{4.10}$$

# 5 Numerical results

In this chapter, the different results obtained from the numerical algorithm developed in [34] will be presented and discussed. The first part of this analysis is focused on pressure driven flows in horizontal channels. In the second part, we will compare these results with gravity driven flows in vertical channels. We will finish with a comparison with granular media. The algorithm has been adapted in consequence for both cases.

## 5.1 Fixed physical parameters

We will work with the same physical parameters used in the article on which our numerical algorithm is based. The fluid is a mixture of glycerin and water and the solid particles are made of silica. The inter-granular stress parameter $\beta_0$ and the diffusivity constant of the configuration stress tensor $\gamma_0$ are fixed to the same values from [33], where the authors calibrated these values with respect to experimental data. These two parameters should be modified in case we are studying suspensions with another particle diameter D.

Here, we want to stress that it is possible to significantly impact particle migration by modifying these parameters. For example, as seen on figures 5.1 and 5.4, decreasing the configuration pressure coefficient $\beta_0$ or decreasing $\gamma_0$ will increase particle concentration at the center. Indeed, these two parameters are included in the compaction equation and have a direct impact on the particle concentration. Nevertheless, these parameters are intrinsic physical properties of the micro-

structure that are difficultly modified in practice. In general, we want to know the best conditions to induce particle migration in function of these material parameters. In this analysis, we want to focus on parameters that are easy to experimentally modify such as; channel height or flow velocity.

| Parameters | Original value | Unit |
|---|---|---|
| $\mu_f$ | $4e^{-2}$ | Pa s |
| $\rho_f$ | $1.2e^{3}$ | kg/m$^3$ |
| $\rho_s$ | $2.1e^{3}$ | kg/m$^3$ |
| $\phi_{jam}$ | 0.6 | / |
| D | $1e^{-6}$ | m |
| $\beta_0$ | $5e^{-2}$ | Pa |
| $\gamma_0$ | $1e^{-9}$ | N |

Table 5.1: Original fixed parameters

### 5.1.1 Impact of $\beta_0$

$\beta_0$ controls the amplitude of the inter-granular stresses or the resistance of grains to compaction, as seen in equ. 4.9. The value of these inter-granular stresses is increasing with the volume fraction and diverging at $\phi_{jam}$, as an accumulation of particles increase their resistance. At $\phi_{jam}$, this resistance can be arbitrarily large.

As $\beta_0$ is increased, the particle migration is inhibited. An higher granular pressure, induced by higher intergranular stresses, tends to balance the normal stresses pushing the particles at the center. These normal viscous stresses are thus decreasing closer from the wall than before. This is marked when the value of $\beta_0$ is reaching 0.5, on fig. 5.3. As a reminder, the granular pressure, as established in the compaction equation (equ. 3.9), is composed of both the diffusion term and the intergranular stresses. As we can see on fig. 5.2, if this value of $\beta_0$ is over-evaluated, the intergranular stresses will be everywhere bigger than the diffusion term and will be the major term impacting the granular pressure. This is the reason why an estimation of $\beta_0 = 0.05Pa$ seems a good estimation (bottom left on fig. 5.2). At the walls, both the diffusion term and intergranular stresses are vanishingly small while at the center, they are bigger. The diffusion term reaches 10% of F $l_{ref}$, the gradient of pressure driving the flow multiplied by $l_{ref}$. Indeed, we need to

compare non-dimensional quantities and F is expressed in Pa/m. The intergranular stresses are 40 times smaller than F multiplied by $l_{ref}$. We observe that if we set the value $\beta_0$ to 0, we reach a particle concentration around 0.5, which is bounded below $\phi_{jam}$. The particle migration, induced by the normal viscous stresses, is thus not bounded solely by the intergranular stresses.

We also notice that the intergranular stresses have a rather flat profile and are of minor importance compared to the the diffusion term that is spikier at the center. The diffusion term is more sensitive to differences in the volume fraction. An interesting impact of $\beta_s$ is on the bottom right picture of fig 5.2. The intergranular stresses were so big that they completely flattened the volume fraction profile. Thus the diffusion term is smaller compared to the three other cases with smaller $\beta_0$ since the gradients of $\phi_s$ are significantly decreased; $\phi_s \approx \bar{\phi}_s$.

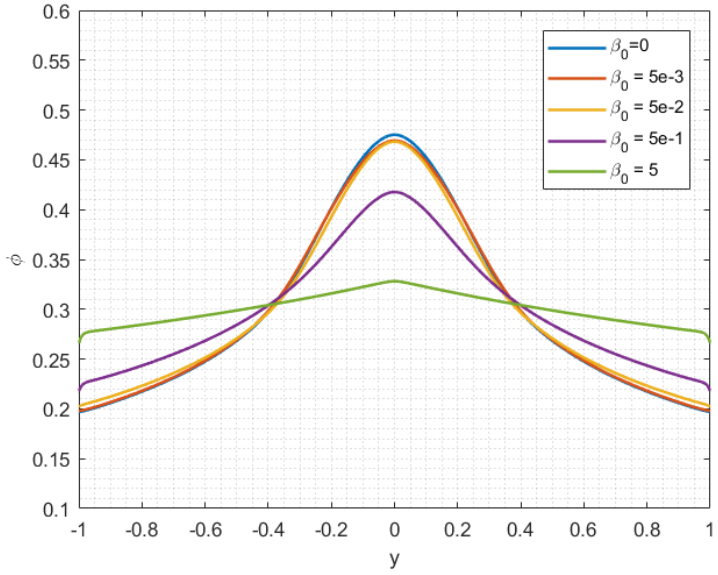


Figure 5.1: The peak of $\phi_s$ is increased with lower $\beta_0$ up until a certain value ($=5e^{-2}Pa$). Standard results (with ł$_{ref} = 20\ \mu m$, $u_{max} = 200\ \mu m/s$ and D=1 $\mu m$)

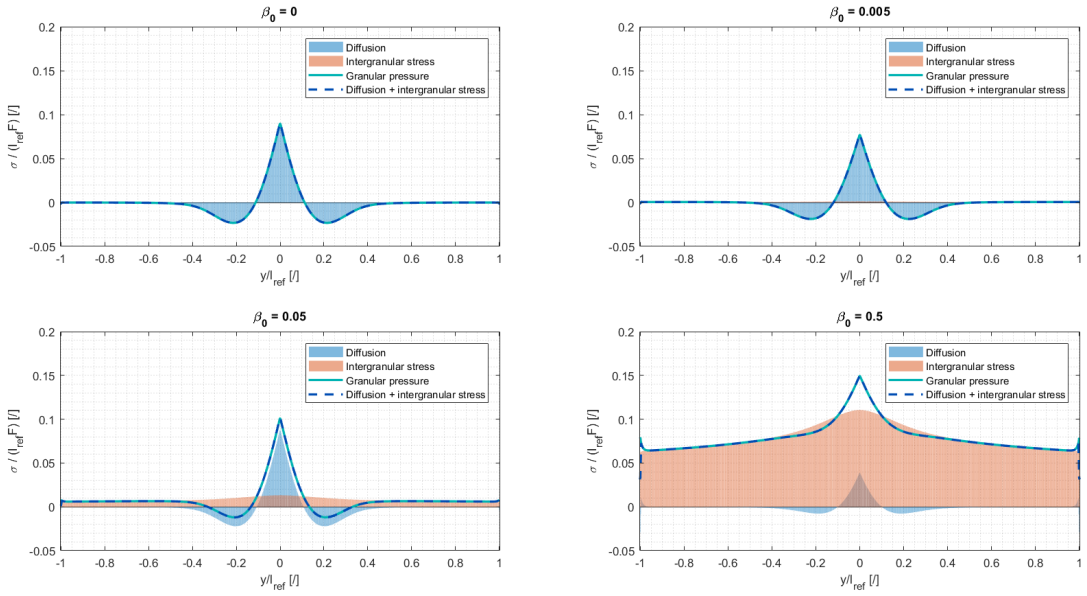


Figure 5.2: Balance in the compaction equation between diffusion term and intergranular stresses, with varying $\beta_0$ - $\bar{\phi}_s = 0.3$

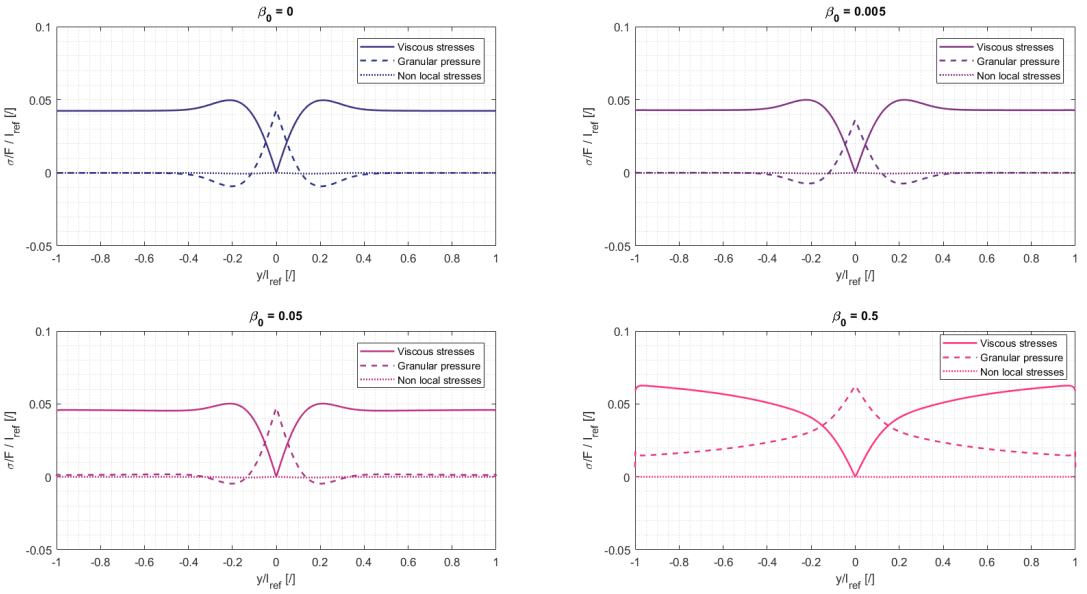


Figure 5.3: Balance in the momentum equation between viscous, non local stresses and intergranular pressure, with varying $\beta_0$ - $\bar{\phi}_s = 0.3$

### 5.1.2 Impact of $\gamma_0$

We then focus on the impact of $\gamma_s$ to the particle migration. In our model, $\gamma_s$ follows a power law with the volume fraction and the amplitude is determined by $\gamma_0$. As we can see on fig 5.4, a decrease of $\gamma_0$ enhances particle migration until the volume fraction reaches $\phi_{jam}$ when $\gamma_0 = 1e^{-12}N$. We observe also that the volume fraction close to the walls remain practically unchanged and that most of the impact is at the center where the peak is more diffuse as $\gamma_0$ increases.

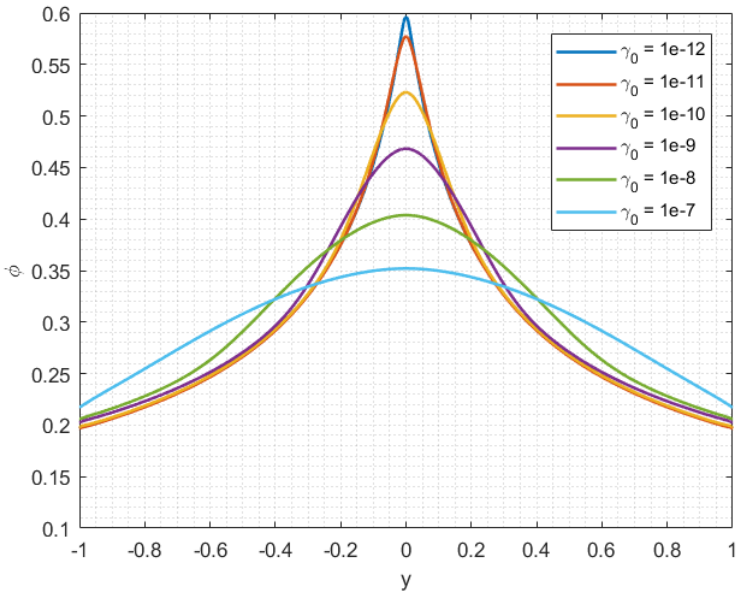


Figure 5.4: The peak of $\phi_s$ is increased with lower $\gamma_0$. Standard results (with $l_{ref} = 20\ \mu m$, $u_{max} = 200\ \mu m/s$ and D=1 $\mu m$)

Compared to the intergranular stresses, $\gamma_0$ really is the parameter that is inhibiting the particle migration and counteracting the normal viscous stresses. Indeed, if $\gamma_0$ is set to a negligible value, particles will agglomerate until the volume fraction reaches $\phi_{jam}$ ($\phi_{s-max} = 0.599$). This enhances the importance of the non-local correction which is essential in order to avoid a constant prediction of $\phi_{jam}$ at the center. Indeed, it has been observed that the central volume fraction should typically decrease to 0.4 for $\bar{\phi}_s = 0.2$.[13] This non-local approach with ad-hoc parameters is thus primordial to evaluate the volume fraction at the center correctly.
We see on fig. 5.5 that the non-local stresses are much smaller than the viscous

stresses and the intergranular pressure. For small values of $\gamma_0$, the normal viscous stresses are always bigger than the granular pressure except at at the center. As $\gamma_0$ is increased, the granular pressure increases further away from the center, which has a direct impact on the normal viscous stresses. The impact of $\gamma_s$ is in fact significant in the compaction equation via the diffusion operator. Indeed, $\gamma_s$ is acting as a diffusion constant that controls the amplitude of the volume fraction gradients in region of clustering. By doing a study of the balance between the diffusion term and the intergranular stresses, it is clear that the diffusion term has a major impact at the center of the channel on the intergranular pressure compared to the intergranular stresses.

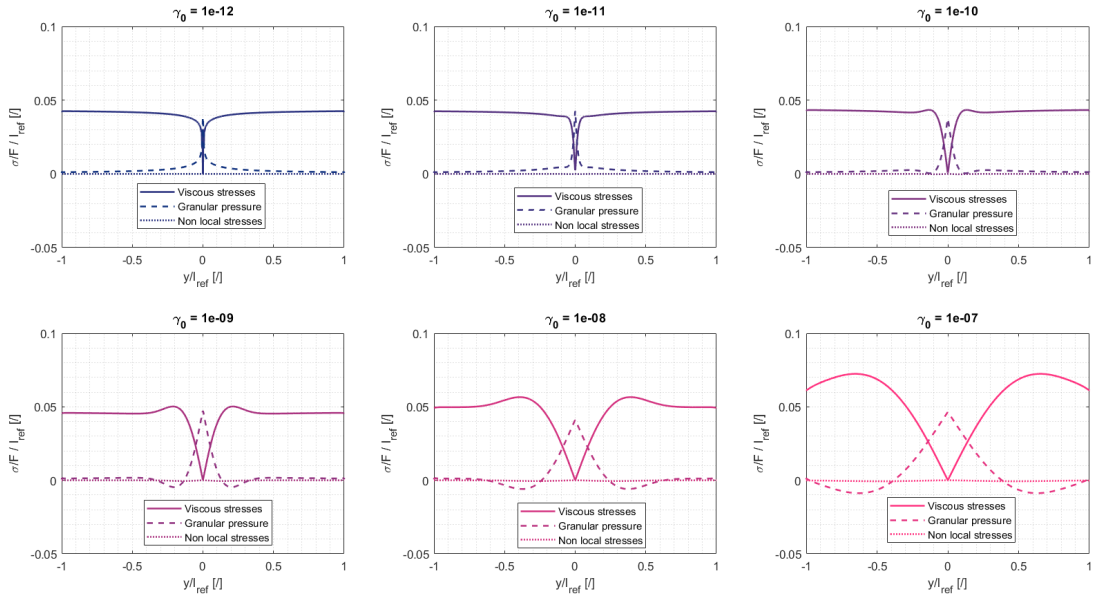


Figure 5.5: Balance in the momentum equation between viscous, non local stresses and intergranular pressure, with varying $\gamma_0$ - $\bar{\phi}_s = 0.3$

As seen on fig 5.6, on the top left figure, the diffusion term is minimal and smaller than the intergranular stresses that have an higher impact on the granular pressure. Nevertheless, these intergranular stresses do not bound the volume fraction below $\phi_{jam}$. As $\gamma_0$ is increased by several orders of magnitude, the diffusion term is increasing and supplanting the intergranular stresses. It also widen the peak of granular pressure along the channel. A good compromise in flows of suspensions

with particles of a diameter of 1 $\mu m$ is to remain with $\gamma_0 = 1e^{-9}N$.

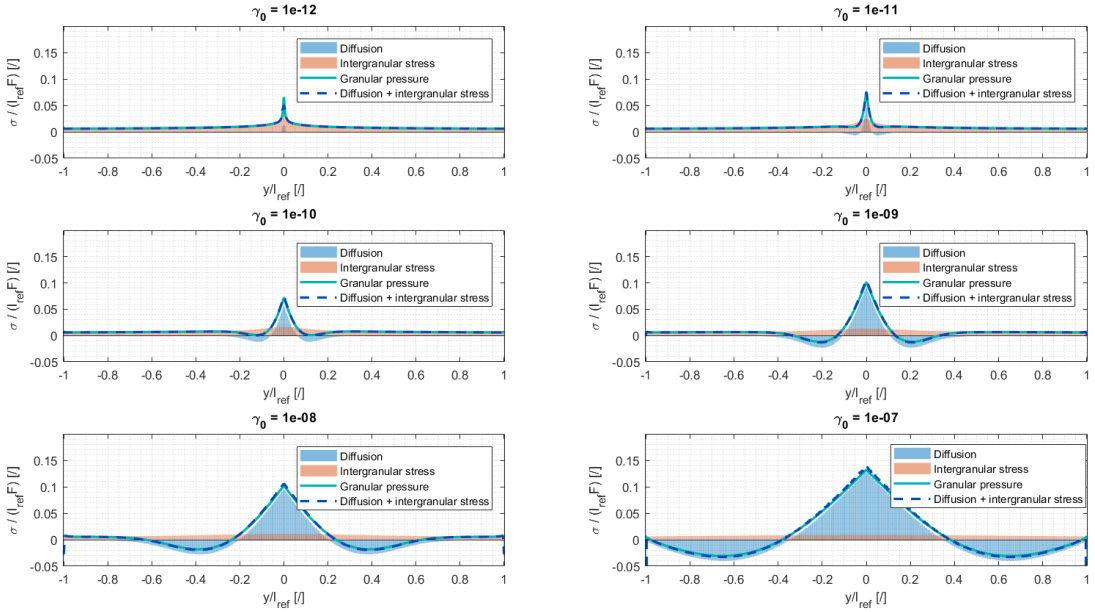


Figure 5.6: Balance in the compaction equation between the diffusion term and intergranular stresses, with varying $\gamma_0$, non dimensionalized by F * $l_{ref}$ - $\bar{\phi}_s = 0.3$

## 5.2 Horizontal channels - Pressure driven flows

### 5.2.1 Comparison with experimental results

A good way to evaluate the model we are using is to compare the results with experimental measurements. To proceed, we will use Gilchrist experiments. [8] These were carried out with Poiseuille pressure driven flows in a micro-channel of an half height of 20 $\mu m$ and particles of a diameter of 1 $\mu m$. The authors imposed a constant velocity at the center (= 200 $\mu m/s$) and it then determines the Reynolds number of the flow (= $1.2e^{-4}$). In order to match $u_{max}$, the equivalent center-line velocity of the single phase flow, we must make the computations with the right pressure gradient, which was not mentioned in the article. This pressure gradient is found with an equivalent of equation 4.4, where $\mu_f$ is replaced by the apparent viscosity $\mu_{susp}$, constant when $\bar{\phi}_s$ is constant. To each pressure gradient,

the algorithm computes a corresponding $u_{max}$ by taking into account mesoscopic phenomena.

We can observe that the numerical results are correctly matching with Gilchrist experiments. A small difference between the two is occurring at the boundaries of the wall. Indeed, the experiments are predicting a drastic decrease of the particle volume fraction at the vicinity of the wall. The numerical results are more mitigated, they compute a volume fraction of 0.3 at the wall for $\bar{\phi}_s = 0.4$ and 0.2 for $\bar{\phi}_s = 0.3$. This could be explained due to the physical difficulty to measure the particle concentration very close to the wall. The discrepancies between the two results are happening for a very small distance, in the order of magnitude of a few particle diameter. This explains why the particle concentration at the center is slightly higher than the experiments since the volume fraction profile must respect the average volume fraction condition.

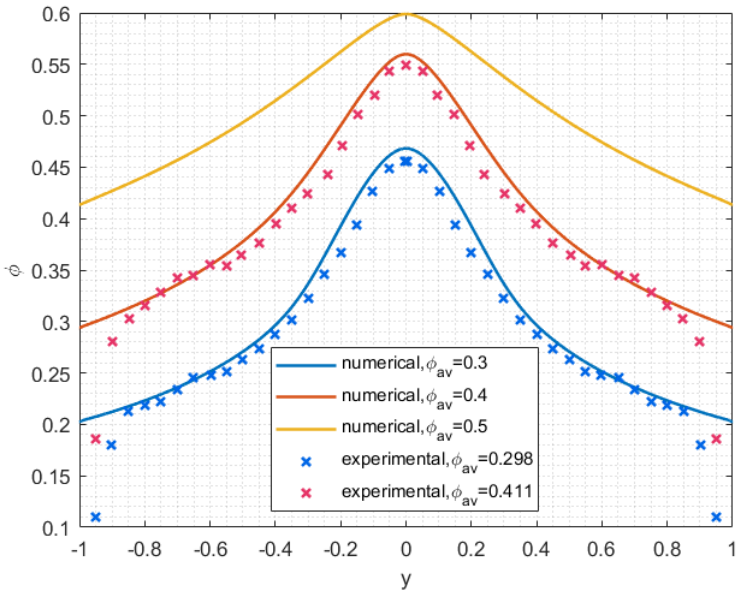


Figure 5.7: Comparison between Gilchrist results and our numerical simulation, D=1$\mu m$, $l_{ref} = 20\mu m$, $u_{max} = 200\mu m/s$

### 5.2.2 Effect of the volume fraction

We note that the apparent viscosity of the whole suspension is increasing with an higher $\bar{\phi}_s$. In order to have the same velocity at the center, when $\bar{\phi}_s$ increase from 0.3 to 0.4, we have to increase the pressure gradient F by 60%. When the average particle concentration is 0.5, the pressure gradient must be nearly 4 times bigger than it was at $\bar{\phi}_s = 0.3$. Here, we want to stress that the apparent viscosity at $\bar{\phi}_s = 0.2$ is already 7 times bigger than the fluid's ($\bar{\phi}_s = 0$).

| $\bar{\phi}_s$ | F [Pa/m] | $\mu_{susp}$ [Pa s] |
|---|---|---|
| 0.2 | $-2.73e^5$ | 0.273 |
| 0.3 | $-3.83e^5$ | 0.383 |
| 0.4 | $-6.21e^5$ | 0.621 |
| 0.5 | $-1.44e^6$ | 1.44 |

Table 5.2: Pressure gradient and apparent viscosity for varying $\bar{\phi}_s$ - $l_{ref} = 20\ \mu m$ and $u_{max} = 2e^{-4}$ m/s

This is due to the increase of intergranular contact and thus of granular viscous dissipations. This is especially the case in the center where it also induces a blunting of the velocity profile, see fig 5.8. We then expect the granular viscous stresses to have a significant impact on the total dissipations.

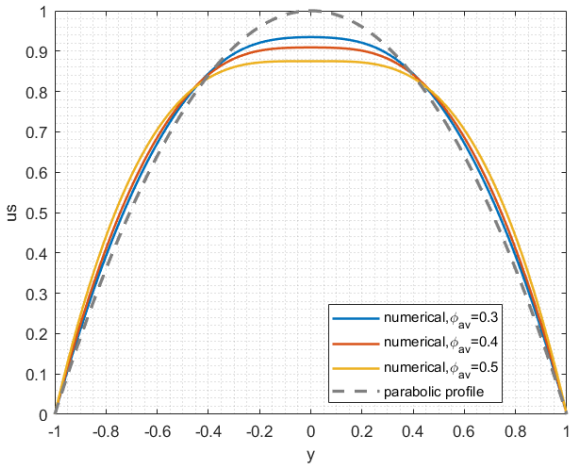


Figure 5.8: Blunting of the velocity profile is more marked for higher $\bar{\phi}_s$ since the accumulation of particles at the center increases the viscosity of the suspension

We evaluate the two viscous stresses by doing the sum of the two equations of the momentum balance along x (equ. 3.6 & 3.7). The drag term disappears and we can find a balance between the fluid and granular viscous stresses:

$$F = \frac{1}{Re}\frac{d}{dy}\left((1-\phi_s)\frac{du_f}{dy}\right) + \frac{1}{Re}\frac{d}{dy}\left(\phi_s \mu_s \frac{du_s}{dy}\right) \tag{5.1}$$

This balance is represented on fig 5.9. At $\bar{\phi}_s = 0.2$, most of the viscous dissipation is happening in the fluid and the granular viscous stresses are only significant at the center. For $\bar{\phi}_s = 0.5$, most of the viscous stresses are granular and due to particles interactions, especially at the center where there is no fluid viscous dissipation.
In fact, the fluid viscous stresses are not diminishing. Their impact compared to F is just smaller. If we did the non-dimensionalisation with the pressure gradient used for $\bar{\phi}_s = 0.2$, the fluid viscous stresses would have the same order of magnitude except at the center. As we increase $\bar{\phi}_s$, we have to increase the pressure gradient to overcome the granular viscous stresses that add themselves to the total viscous dissipation.

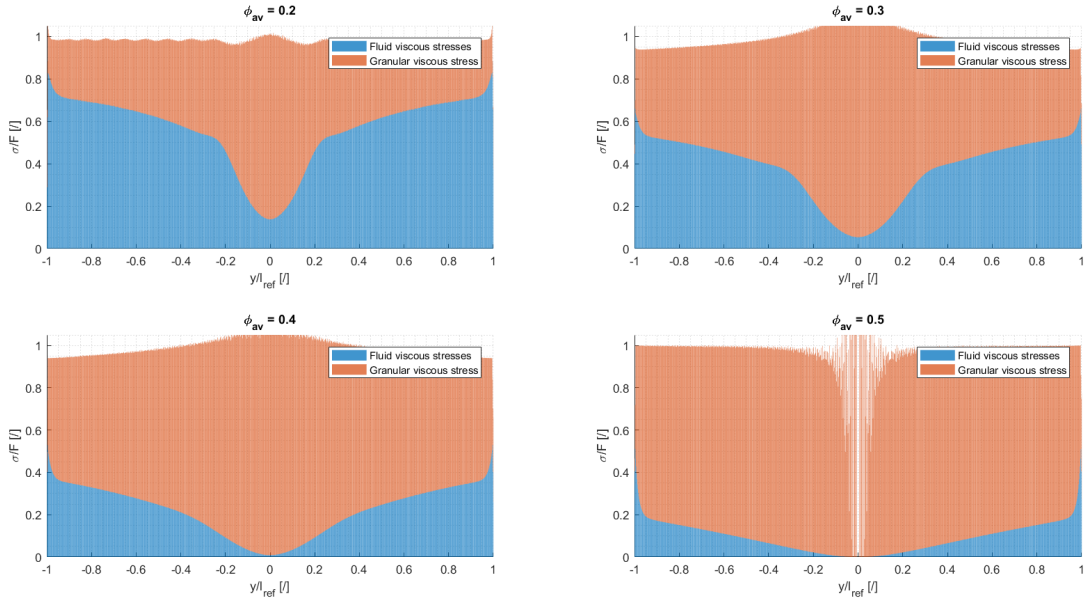


Figure 5.9: Balance of the viscous stresses for varying $\bar{\phi}_s$

### 5.2.3 Effect of the pressure gradient

Gilchrist and Gao observed that the maximum degree of segregation is achieved in a straight channel once the maximum packing fraction is reached at the center of the channel.[8] This best segregation is achieved in this case when $\bar{\phi}_s$ is equal to 0.5 as seen on fig 5.8. They also claim that the mixing and the separation can be tailored by adjusting both the channel geometry and the suspensions properties such as $\bar{\phi}_s$ or $\mu_f$.
We will then analyse how we can achieve maximal segregation and how will the particle migration be affected if we increase the height of the channel and the velocity at the center. This will tailored by the pressure gradient and can be simplified as an increase of the Reynolds number of the flow if we keep the fluid properties $\rho_f$ and $\mu_f$ constant.

$$Re = \frac{\rho_f u_{max} l_{ref}}{\mu_f}$$

Indeed, we want to increase the flow rate as Gilchrist experiments remain a small scale application. Nevertheless, $u_{max}$ and $l_{ref}$ do not impact the flow in the same way. We will analyse separately the impact of these two parameters on the particle migration.

#### Impact of $l_{ref}$ - decrease of the pressure gradient

At first, we want to know what happens when we increase the channel height. To keep the velocity $u_{max}$ constant, we have to decrease the pressure gradient F in function of $l_{ref}$, which will then decrease quadratically. We observe that doubling the channel half-height from 20 to 40 $\mu m$ increases the particle peak to 0.48 at the center. However, after that, we encounter a non physical behaviour during our simulations; the fluid velocity becomes negative. After some investigation, we noticed that it was caused by a too stiff drag coefficient. In order to avoid this behaviour, we had to diminish the drag coefficient $\delta$ by a shrinkage factor $\epsilon$. This factor is mentioned on the figures 5.10 and 5.11; we had to go from 0.35 to 0.1 when going to channel from half-height of 80 to 160 $\mu m$. This will be further discussed in the next section dedicated to the drag law.

| $l_{ref}$ [$\mu m$] | $u_{max}$ [mm/s] | F[Pa/m] | Re | $\phi_{max}$ |
|---|---|---|---|---|
| 20 | 0.2 | $-3.83e^5$ | $1.2e^{-4}$ | 0.468 |
| 40 | 0.2 | $-9.5e^4$ | $2.4e^{-4}$ | 0.48 |
| 80 | 0.2 | $-2.4e^4$ | $4.8e^{-4}$ | 0.482 |
| 160 | 0.2 | $-6e^3$ | $9.6e^{-4}$ | 0.467 |

Table 5.3: To vary $l_{ref}$, F decreases quadratically in order to keep $u_{max}$ constant

The observed behaviour however shows that increasing to 80 or 160 $\mu m$ when keeping $u_{max}$ constant does not increase the peak of $\phi_s$ at the center. This corroborates the importance of the shear rate $\dot{\gamma}$. Indeed when $l_{ref}$ increases with constant $u_{max}$, the apparent shear rate is diminishing.

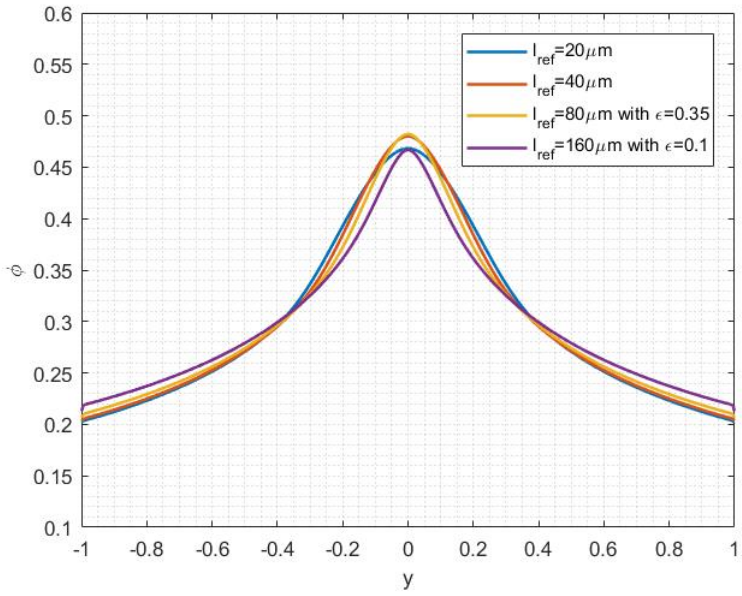


Figure 5.10: The maximum $\phi_s$ is constant and equals to 0.48. Only the spikiness is evolving; as $l_{ref}$ increases, the particles are slightly more distributed along the channel - $u_{max} = 200\ \mu m/s$

In this case, to understand in depth the behaviour of the suspension and why the particle concentration seems to be bounded below 0.48, we need to study the balances of stresses in the momentum equation along y. We will use equ. 3.8 containing three different terms; the normal viscous stresses $\frac{\mu_n \phi_s}{Re} |\frac{du}{dy}|$, the intergranular pressure multiplied by the volume fraction $p_s \phi_s$ and the non-local

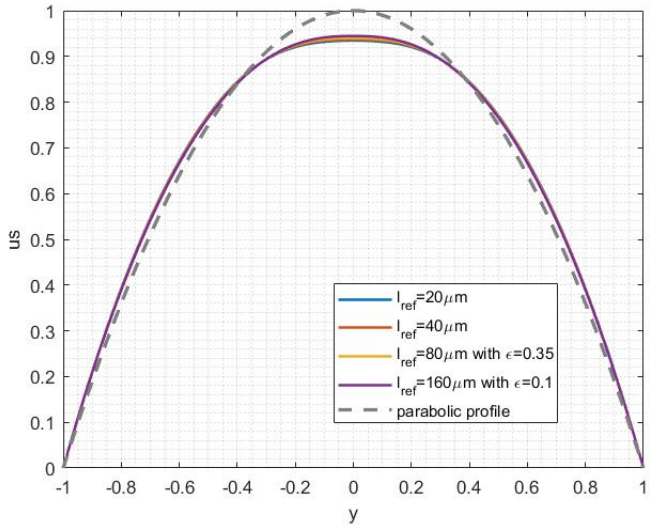


Figure 5.11: The impact of an increase of $l_{ref}$ is not significant to the velocity profile

stresses $\gamma_s \left(\frac{d\phi_s}{dy}\right)^2$. This is a convenient approach because thanks to the modelling, we have a access to a lot of information; the normal stress viscosity, the local shear rate or $\gamma_s$. We then have a precise view of which stresses are predominant.
As briefly mentioned in section 6.1.2, the non-local stresses are everywhere very small compared to the two other stresses. There is thus a balance between the variation in function of y of the intergranular pressure and the normal viscous stresses. This can be clearly seen on fig 5.13. The granular pressure, multiplied by $\phi_s$, is a mirror reflection of the viscous stresses.

What we also notice is that with increasing $l_{ref}$, both the viscous terms and the intergranular pressure, while reaming constant at the wall and at the center, tend to diffuse along y. As $l_{ref}$ increases, the diminishing and increasing are less sharp. While the viscous stresses were everywhere constant and equals to 5% of the product F $l_{ref}$ and decreasing to zero at the center only from 0.2 $l_{ref}$ for $l_{ref} = 20\mu m$, the decrease to zero at the center is less sharp for $l_{ref} = 160\mu m$ and starts already at the wall. We also observe a slight increase of the viscous stresses at around 0.4 $l_{ref}$ for the two first cases ($l_{ref} = 20$ & $40$ $\mu m$).
This can be explained by the intergranular stresses that are becoming of bigger

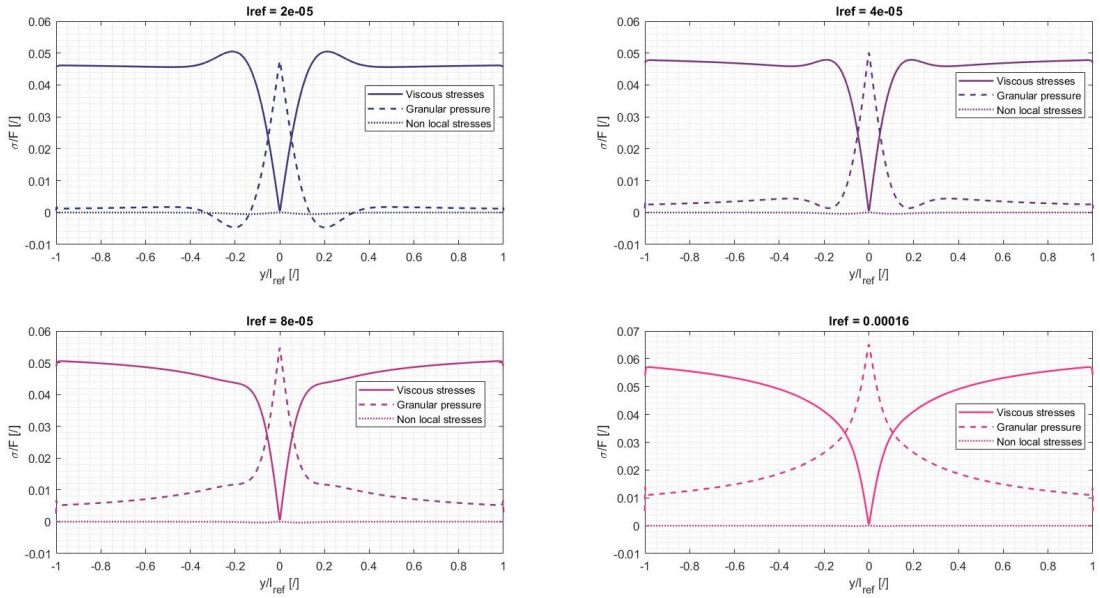


Figure 5.12: Balance of stresses along y for varying $l_{ref}$ at $u_{max} = 200\ \mu m/s$

importance in the compaction equation as $l_{ref}$ increases, as seen on fig 5.13. Indeed, for the two smallest channel heights, the diffusion term in blue is bigger than the intergranular stresses in red, while it is the contrary for two higher channels; the intergranular stresses are responsible of most of the intergranular pressure.
In general, we can assume that the diffusion term is predominant when we observe the oscillating pattern between negative and positive values, which is characteristic of the diffusion term. This is originated from the inflexion point of the volume fraction gradient, that happens in general at $l_{ref} \approx \pm 0.4$. We are thus in the same kind of behaviour than in section 6.1.1 where intergranular stresses were bigger than the diffusion term when $\beta_0$ was equal to 0.5. In this previous case, the intergranular stresses were predominant because $\beta_0$ was high. In our case, the intergranular stresses remain constant but are higher compared to the product F $l_{ref}$ which is increasing since F is decreasing quadratically with $l_{ref}$ when $u_{max}$ and $\mu_{susp}$ remain constant.

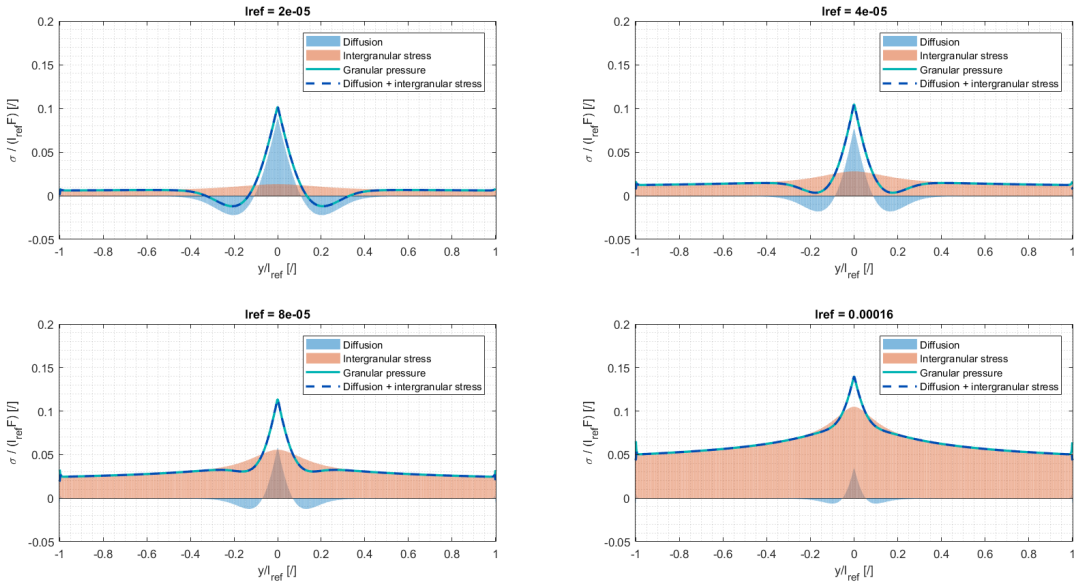


Figure 5.13: Balance of terms in the compaction equation for varying $l_{ref}$ at $u_{max} = 200\ \mu m/s$

**Impact of $u_{max}$ at $l_{ref} = 20\mu m$ - increase of pressure gradient**

Then, we observe how the same variation of the Reynolds number induces a different behaviour when we are modifying the central velocity only. This increase is induced by an increase of the pressure gradient with the same method used to match the central velocity at 200 $\mu m/s$ when comparing in 6.2.1. We can see that we are able to reach higher values of Reynolds number, by increasing $u_{max}$. We reach $u_{max} = 6.4e^{-3} m/s$ and $\phi_{max} = 0.56$.

| $u_{max}$ [mm/s] | $l_{ref}$ [$\mu m$] | F[Pa/m] | Re | $\phi_{max}$ |
|---|---|---|---|---|
| 0.2 | 20 | $-3.83e^5$ | $1.2e^{-4}$ | 0.468 |
| 0.4 | 20 | $-7.66e^5$ | $2.4e^{-4}$ | 0.49 |
| 0.8 | 20 | $-1.53e^6$ | $4.8e^{-4}$ | 0.511 |
| 1.6 | 20 | $-3.06e^6$ | $9.6e^{-4}$ | 0.531 |
| 3.2 | 20 | $-6.13e^6$ | $1.92e^{-3}$ | 0.55 |
| 6.4 | 20 | $-1.23e^7$ | $3.84e^{-3}$ | 0.56 |

Table 5.4: Impact of pressure gradient with $l_{ref} = 20\ \mu m$

| $u_{max}$ [mm/s] | $l_{ref}$ [$\mu m$] | F[Pa/m] | Re | $\phi_{max}$ |
|---|---|---|---|---|
| 0.2 | 40 | $-9.5e^4$ | $2.4e^{-4}$ | 0.48 |
| 0.4 | 40 | $-1.9e^5$ | $4.8^{-4}$ | 0.506 |
| 0.8 | 40 | $-3.82e^5$ | $9.6^{-4}$ | 0.53 |
| 1.6 | 40 | $-7.64e^5$ | $1.92^{-3}$ | 0.55 |
| 3.2 | 40 | $-1.53e^6$ | $3.84^{-3}$ | 0.568 |
| 6.4 | 40 | $-2.97e^6$ | $1.54^{-2}$ | 0.582 |

Table 5.5: Impact of pressure gradient with $l_{ref} = 40\ \mu m$

**Impact of $u_{max}$ at $l_{ref} = 40\mu m$ - increase of pressure gradient**

We want to increase the height of the channel in order to increase the mass flow rate but here we are limited by the drag law. We decide to increase $l_{ref}$ up to the limit where we do not need to modify the drag coefficient $\delta$, which is $l_{ref}$= 40 $\mu m$. We are then left with a maximal values of $l_{ref}$ and $u_{max}$ that lead to a Reynolds number of 1.54e-2. These two experiments of increasing $u_{max}$ at different $l_{ref}$ show that we have more room of improvement with varying $u_{max}$. We are able to reach a velocity of $6.4e^{-3}$ m/s which is 32 times the original velocity. However, due to limitations of the drag law, we have only been able to multiply by 2 the channel height.

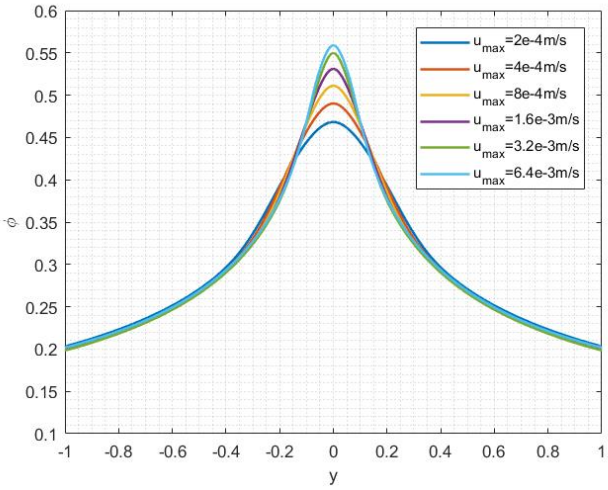


Figure 5.14: Modifying $u_{max}$ and keeping $l_{ref}$ constant by adapting the pressure gradient F increase particle migration until $\phi_s = 0.56$ when $l_{ref} = 20\mu m$

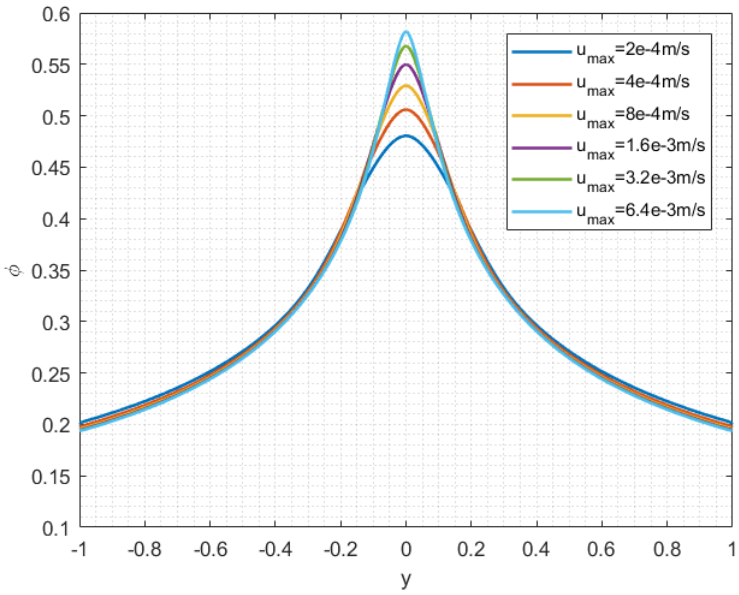


Figure 5.15: Modifying $u_{max}$ increase particle migration until $\phi_s = 0.58$ when $l_{ref} = 40\ \mu m$

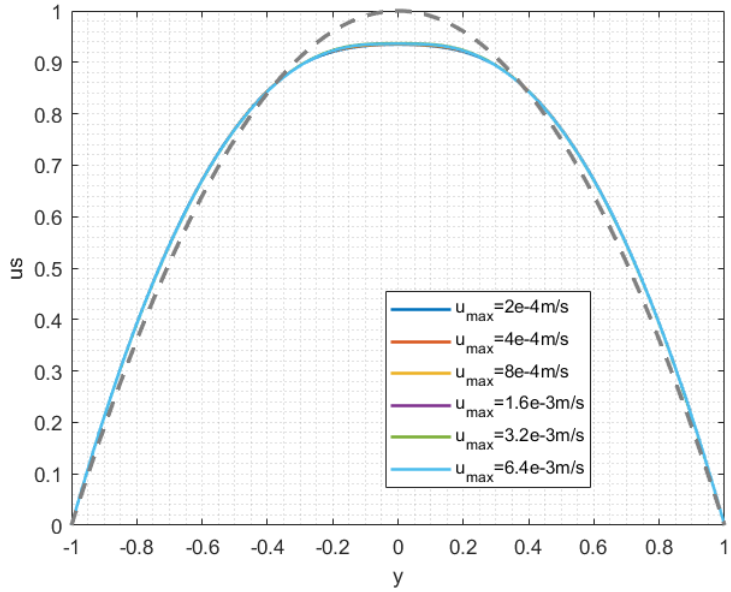


Figure 5.16: The impact of an increase of $u_{max}$ is not significant - $l_{ref} = 20\mu m$

**Parallel between increase of $u_{max}$ and decrease of $\gamma_0$**

Interestingly enough, we can make a parallel between the behaviour of an increase of $u_{max}$ with an increase of F with the behaviour of the suspension when varying $\gamma_0$ between $1e^{-9}$ and $1e^{-11}N$. Indeed, in both cases, the particle volume fraction at the wall remains mainly unchanged while $\phi_s$ at the center is seen to reach higher values with increasing values of $u_{max}$ or decreasing values of $\gamma_0$.

We once again study the terms in the compaction equation. We remember that in fig. 5.6, when $\phi_s$ was the highest, it was for the lowest value of $\gamma_0$ ($=1e^{-11}N$) and that the granular pressure was mainly governed by intergranular stresses and equals to 5% of the product F $l_{ref}$ at the center. With increasing $\gamma_0$, the diffusion term was taking more importance and inhibiting the particle migration until the diffusion term was the main term impacting $p_s$, with central values above 10% of F $l_{ref}$ ($\gamma_0 = 1e^{-9}N$).

However, in the case of increasing $u_{max}$, as seen on fig 5.18, it is different. For the highest particle volume fraction, at $u_{max} = 6.4$ mm/s, the intergranular stresses are negligible compared to the diffusion term. The granular pressure was thus completely caused by the sharp increase of $\phi_s$ gradient instead of the intergranular stresses. For this value of $u_{max}$, $p_s$ is governed solely by the term containing $\gamma_s$, and is equals to 5% of F $l_{ref}$. Then, with diminishing values of $u_{max}$ (and thus of F), the intergranular stresses are taking more importance and the granular pressure rises until 10% at the center.

In conclusion, the two cases are similar because the equivalent granular pressure and the normal viscous stresses have a similar profile. However, the decrease from 10% of F $l_{ref}$ to 5% in both cases, when increasing $u_{max}$ or decreasing $\gamma_0$ is due to a decrease of the importance of the intergranular stresses or the diffusion term respectively.

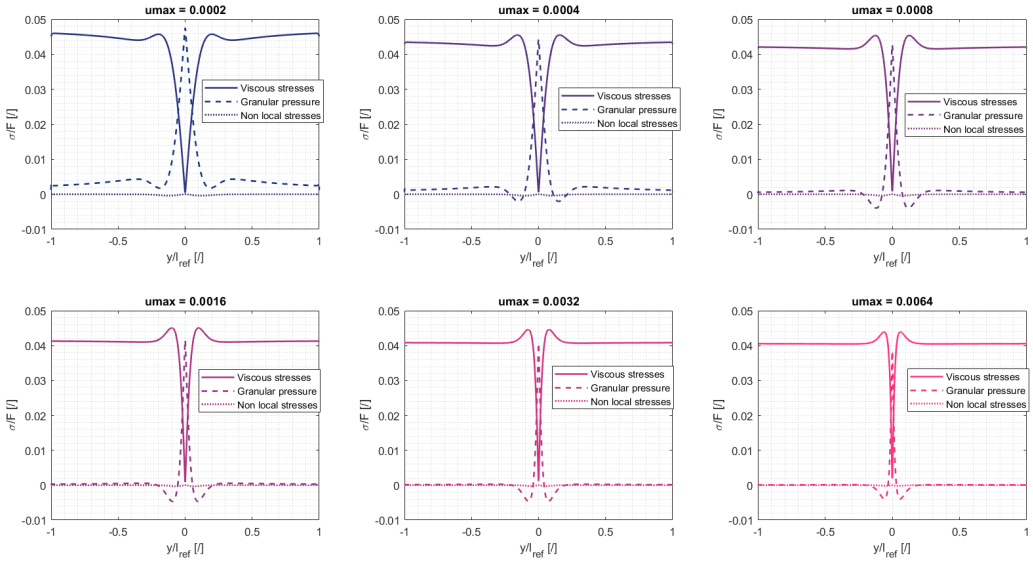


Figure 5.17: Balance of the stresses in the momentum equation along y with varying $u_{max}$ at $l_{ref} = 40\mu m$

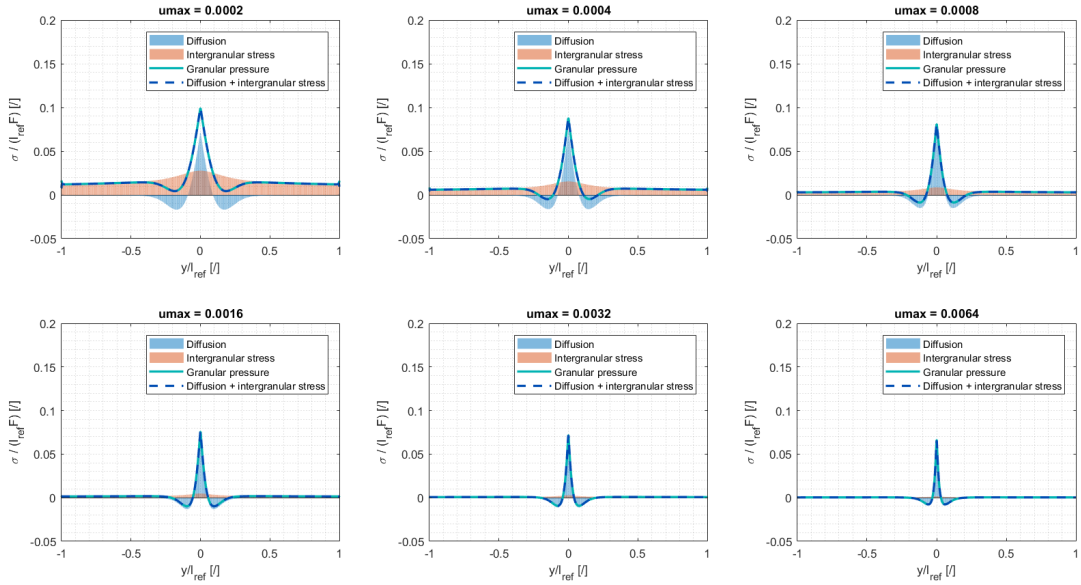


Figure 5.18: Balance of the terms in the compaction with varying $u_{max}$ at $l_{ref} = 40\mu m$

### 5.2.4 Effect of the drag law

We have seen in the previous section that the draw law has an negative effect when the channel height is increased. As explained in the section dedicated to the governing equations, the drag coefficient is the *Robin Hood* of the velocity. When one phase is going faster than the other one, $\delta$ acts to balance the velocities. It behaves as an added forcing term for the slowest phase and a subtraction of the forcing term for the fastest phase. In the case encountered in section 6.2.1, when we increase $l_{ref}$, the coefficient $\delta$ is over-evaluated and is then so stiff that it overbalances the two phases velocities. A small difference of the two velocities is creating an instability resulting in the fluid velocity becoming negative. Since the correction is based on an absolute value of the differences, the drag coefficient is still increasing and unbalancing the two phases even further. The code then crashes because it is reaching infinite values for the fluid velocity.

#### Shrinkage factor

The solution is to use a shrinkage factor $\epsilon$ that diminishes the drag coefficient. We then avoid an over-evaluation of $\delta$ and numerical troubles. Nevertheless, this $\epsilon$ does not affect the physical behaviour. Indeed, as seen at 5.19 a diminution up to $\epsilon = 0.01$ does not affect the difference between $u_s$ and $u_f$.

#### Comparison with another drag law

We then decided to analyse if the over-evaluation of $\delta$ was coming from the drag law. We decided to replace the current drag law (HKL correlation) by another one used in the literature in order to compare the differences. The other correlation has been developed by Gobin et al in 2003. [11] The authors are using a combination of two empirical correlations developed in the 50's and 60's; Wen & Yu [46] and Erdun [6], two correlations widely used in the field. Wen & Yu is used for semi-dilute regimes while Erdun's is better for dense regime. According to Simonin et al. [43], this correlation is a good application for the fluid-particle momentum transfer modelling and confirmed by DNS such as Lattice Boltzmann method. This correlation is of special importance in the modelisation of gas-solid fluidised beds reactors.

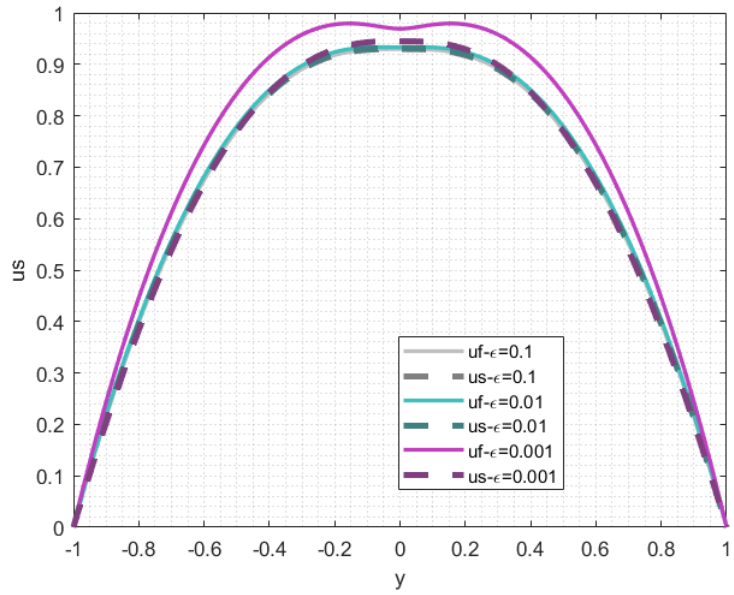


Figure 5.19: The shrinkage factor $\epsilon$ must decrease $\delta$ by 3 orders of magnitude in order to induce a difference in the phase velocities - $l_{ref} = 80\mu m$ - $u_{max} = 200\mu m/s$

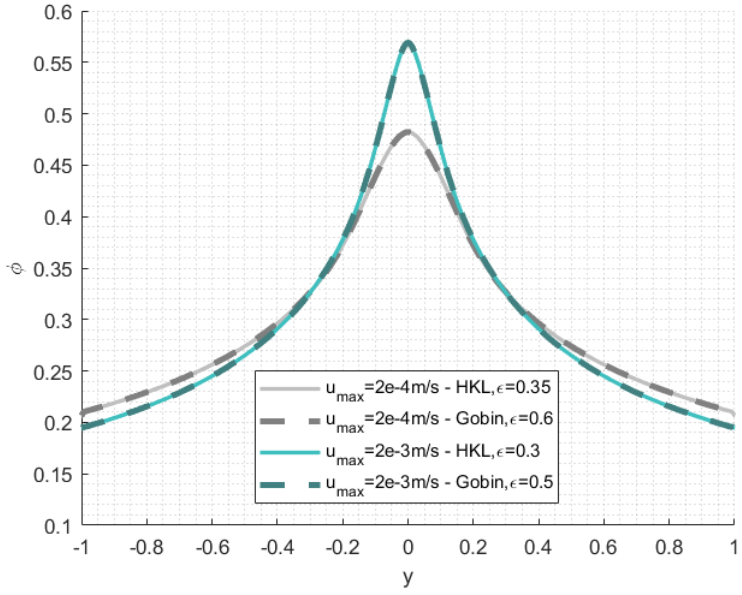


Figure 5.20: Comparison of HKL with Gobin et al correlation - there is no significant difference - $l_{ref} = 80\mu m$

The used formula is:

$$F_{gob} = \begin{cases} \mathrm{F}_{wy}, & \text{if } \phi_s < 0.3 \\ \mathrm{F}_{erg}, & \text{otherwise} \end{cases} \quad \text{with}$$

$$F_{erg} = \frac{150}{18}\frac{\phi_s}{(1-\phi_s)^2} + \frac{7}{72}\frac{Re_p}{(1-\phi_s)^2}$$

$$F_{wy} = (1 + 0.15Re_p^{0.687})(1-\phi_s)^{-3.65}$$

$$\delta = \frac{18F(1-\phi_s)^2\mu_f}{D^2}$$

We ran the simulations with a channel half-height of 80 $\mu m$, with a shrinkage coefficient $\epsilon$. We also compare two different cases; the original velocity $u_{max} = 200\mu m/s$ and $u_{max} = 2mm/s$. We notice that there are no significant improvement if we change the drag law. With Gobin's correlation, we however notice that the $\delta$ coefficient is a bit less overevaluated. For the same channel height, we can stick with an higher shrinkage factor (0.6 instead of 0.35 at $u_{max} = 200$ $\mu$m/s).

### 5.2.5 Effect of the domain size

In this section, we will analyse to what extent the choice of the domain size impacts the simulations. For example, when we are doing computations for wider channels, we want to know what is the minimum number of grid points we need to choose. We observed on fig 5.22 that for a channel half-height of 80 $\mu m$, n = 100 is not a sufficient number of grid points since the peak is cusped. We decided to remain with n = 1000 which is a good compromise between accuracy and CPU time for the channel heights we are studying. In general the critical point where we need more grid points is at the peak of particle volume fraction when it is close to $\phi_{jam}$. Indeed, it is the point where the gradients are the biggest and we then need more points to achieve accuracy. For these simulations, it is also important to have a sufficient number of grid points in order to have accuracy for the granular pressure which also has a spiky profile. The error must remains in the order of 0.1 - 0.01 %.

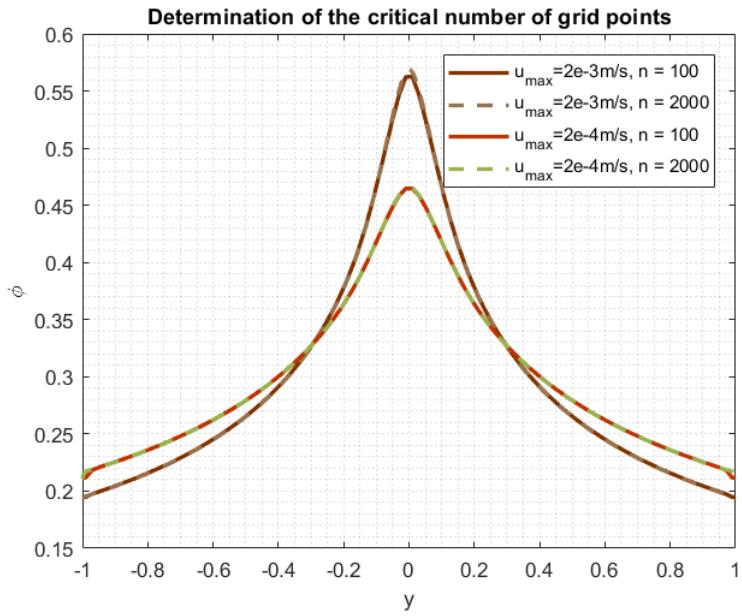


Figure 5.21: Comparison of the particle concentration with two different number of grid points, $ł_{ref} = 80\mu m$

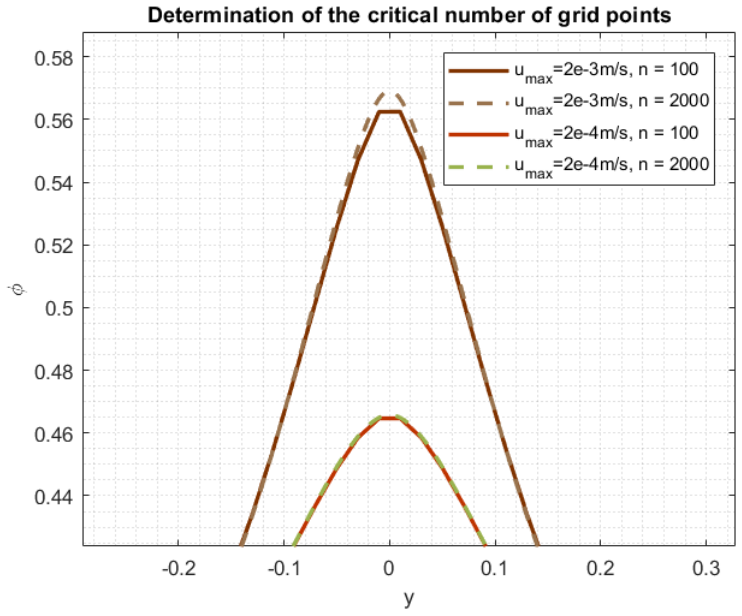


Figure 5.22: Zoomed version of fig 5.21, at n = 100, the peak of $\phi_s$ is flattened when $u_{max} = 2e-3m/s$ - $ł_{ref} = 80\mu m$

### 5.2.6 Effect of the boundary conditions

Non colloidal suspensions can often be modelled as Newtonian fluids having an effective viscosity $\mu_{susp}$, provided that D, the diameter of the particles, is smaller than the so-called macro-scale. But such continuum description is not valid in the vicinity of the wall, over distance $\mathcal{O}$(D), where the discrete nature of the suspension influences its flow behaviour in a significant way.[18] Slip essentially reduces the drag coefficient for fluids flowing through a confined geometry thereby enhancing the velocity and the flow rate. The boundary conditions are thus critical and an area of active study. In this section, we will analyse how and when we have to modify the boundary conditions in order to obtain more realistic results. As seen on fig 5.23, there are three different practicable boundary conditions; no slip, true and apparent wall slip. [23]

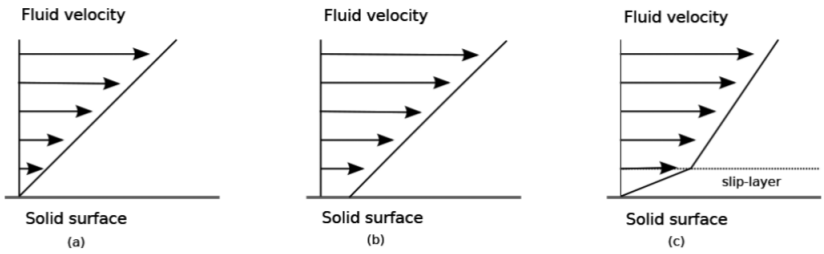


Figure 5.23: Schematic presentation of different boundary conditions: a) no slip b) true wall slip c) apparent wall slip [48]

The main difference between true and apparent wall slip is that for the apparent slip the velocity is null at the wall while it is not the case for the true wall slip.
In the apparent wall slip, we define a slip *layer* which is the layer close to the wall where the velocity is increasing faster due to a depletion of particles. The hypothesis in the apparent wall slip is that the thickness of the slip layer does not change with the shear rate.
In both cases, we can also define an apparent slip *length* $l_{slip}$ that represents the distance to the wall at which the velocity profile extrapolates to zero. It is established from the literature that the slip length is increasing with the volume fraction [10] while the slip layer is decreasing with $\phi_s$. [19]

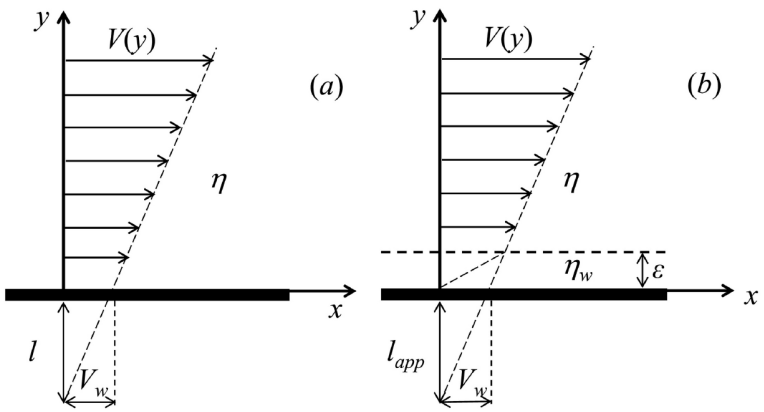


Figure 5.24: Difference between true and apparent wall slip [29] - Both have a slip length (l and $l_{app}$), only the apparent wall slip has a slip layer $\epsilon$ on the figure

### No slip

The simplest way to proceed is to impose zero velocity at the wall as if it is a simple Newtonian fluid. Both the normal and tangential part of the velocity are imposed to zero.

$$\bar{n} \cdot \bar{u} = 0$$
$$\bar{t} \cdot \bar{u} = 0$$

In the case of unidirectional flow, since $\bar{u}_s = u_s(y)\hat{\mathrm{e}}_x$ and $\bar{u}_f = u_f(y)\hat{\mathrm{e}}_x$, the normal velocity is already set to zero.
The boundary condition is thus simply:

$$u_s(1) = u_s(-1) = 0$$

$$u_f(1) = u_f(-1) = 0$$

In the algorithm, it is implemented in a way such that we only have to set the values of the constants $c_{1-u_s}$,$c_{2-u_s}$ and $c_{3-u_s}$ of the equation:

$$c_{1-u_s}u_s + c_{2-u_s}\frac{du_s}{dy} = c_{3-u_s}$$

For example, to impose the impermeability condition to the volume fraction, $\frac{d\phi_s}{dy} = 0$, $c_{1-\phi_s}$ and $c_{3-\phi_s}$ are fixed to 0 and $c_{2-\phi_s}$ to 1.
In the case of no slip boundary condition, $c_{1-u_s}$ is set to 1 and the two others $c_{2-u_s}$ and $c_{3-u_s}$ are set to zero. The method is the same for the constants of the fluid phase. The no slip boundary condition has been applied to all previous results and are of good agreement with Gilchrist results for example.

**True wall slip**

For the true wall slip, the idea is to set the value of the particles at the wall to a certain fraction of $u_{max}$ in order to allow some slip between the granular phase and the wall. According to [9], the wall slip is most marked for dense suspension ($\bar{\phi}_s = 0.5$). For these tests, I decided to apply these new boundary conditions to the same test we use to compare with Gilchrist's experiments. (see section 5.2.1) So, we used D = 1 $\mu m$, $l_{ref} = 20$ $\mu m$ and $u_{max} = 200$ $\mu m/s$. I then apply different fractions of $u_{max}$ to the velocity at the wall. For the implementation of these boundary conditions, we have to define the constants; $c_{1-u_s} = 1$, $c_{2-u_s} = 0$ and $c_{3-u_s} = x_s u_{max}$. $x_s$ is thus evaluated between 0 (no slip) and 0.3. The authors of [9] found that the wall slip velocity for $\bar{\phi}_s = 0.5$ was around 0.2 $u_{max}$. We observe

| $\bar{\phi}_s$ | F [Pa/m] | $u_{slip}$[m/s] |
|---|---|---|
| 0.3 | $-3.66e^5$ | 0.05 $u_{max}$ |
| 0.3 | $-3.47e^5$ | 0.1 $u_{max}$ |
| 0.3 | $-3.27e^5$ | 0.15 $u_{max}$ |
| 0.3 | $-3.19e^5$ | 0.2 $u_{max}$ |
| 0.4 | $5e^5$ | 0.2 $u_{max}$ |
| 0.4 | $-4.42e^5$ | 0.3 $u_{max}$ |
| 0.5 | $-8.33e^5$ | 0.3 $u_{max}$ |

Table 5.6: Effects of slip conditions on F

that since the wall slip velocity induces a further blunting of the velocity profile,

we have to diminish the pressure gradient F if we want to keep the same center-line velocity. This corroborates with the claim of Kroupa et al [26] that the slip could be the origin of shear-thinning and a decrease of the viscosity of the suspension. We also notice that the wall slip condition has a major impact on the $\phi_s$ profile at the boundary. Nevertheless, the rest of the profile is slightly impacted as it does not significantly differ from the original results, see fig 5.7.

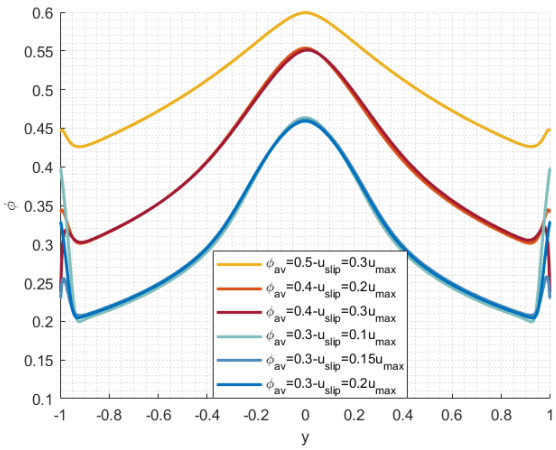


Figure 5.25: True wall slip - Changing the value of the solid velocity at the wall only impacts $\phi_s$ at the wall, not at the center - $l_{ref} = 20\mu m$, $u_{max} = 200\mu m/s$

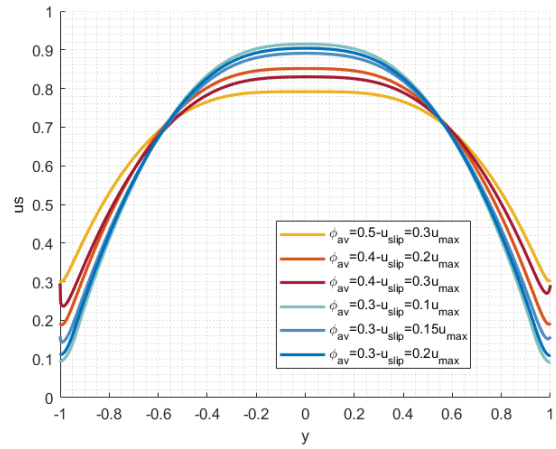


Figure 5.26: True wall slip - Increasing $u_{slip}$ increases the blunting of the velocity profile and thus diminishes the pressure gradient needed to drive the flow

### Apparent slip

Since dense suspension express more complex behaviour than Newtonian fluid, a no-slip boundary condition does not capture the whole behaviour of the flow at the vicinity of the wall. As shear-induced particle migration influences the volume fraction profile, the apparent slip deviates the velocity profiles near the wall. The area where the velocity profile is sharper is called slip-layer and has a thickness $\delta_{slip}$. Instead of fixing a constant value depending on $u_{max}$ as we did for true wall slip, the idea is to fix a constant variation of $u_s$ along y. We are then using a Neumann condition instead of a Dirichlet boundary condition.
Generally, apparent slip is the most observed slip in dense suspensions.[48] The slip arises from a depletion of the particles adjacent to the shearing surfaces because particles can not physically occupy the space adjacent to the wall as effectively as in the bulk fluid.[17, 19] The apparent slip velocity appears to increase with the size of particles and concentration.
The apparent slip velocity is computed with a equation inspired from Newton law. The equation can be found in several papers, I chose the equation 1.19 in [9].

$$\beta_w \delta_{slip} \tau_w = \mu_f (u_{slip} - u_w)$$

where $\beta_w$ is a parameter to match the experimental data, fixed to 1 in the article and $u_{slip}$ is the velocity of the suspension at the wall ($= u_{susp}(1)$). Since in our case $u_w = 0$ and using Kaylon's correlation [19] to estimate the thickness of the slip layer, and by fixing $u_{slip} = 0$ at $\phi_s = 0$:

$$\delta_{slip} = D\left(1 - \frac{\phi_s}{\phi_m}\right)$$

$$u_{slip} = \beta_w D\left(1 - \frac{\phi_s}{\phi_m}\right)\phi \frac{\mu}{\mu_f}\frac{du_{slip}}{dy}$$

We are then left with an expression of the form:

$$u_{slip} - \beta_w D\left(1 - \frac{\phi_s}{\phi_m}\right)\phi \frac{\mu}{\mu_f}\frac{du_{slip}}{dy} = 0$$

In the article, the velocity of the suspension is defined as:

$$u_{susp} = \frac{\rho_f(1-\phi_s)u_f + \rho_s\phi_s u_s}{\rho_{susp}}$$

where $\rho_{susp} = \rho_f(1-\phi_s) + \rho_s\phi_s$ is the average density of the suspension.

$$u_s = u_{susp} + (1 - \frac{\rho_s\phi_s}{\rho_{susp}})(u_s - u_f)$$
$$u_f = u_{susp} - \frac{\rho_s\phi_s}{\rho_{susp}}(u_s - u_f)$$

At the wall, we can still assume that $u_f = 0$. It leads to:

$$u_f(1) = u_f(-1) = 0$$
$$u_s(1) = u_s(-1) = \frac{\rho_{susp}u_{slip}}{\rho_s\phi_s}$$

In the code, the apparent slip is adjusted by keeping $c_{1-u_s} = 1$ (same as no slip), $c_{3-u_s} = 0$ and setting $c_{2-u_s}$ to

$$c_{2-u_s} = -\beta_w D\left(1 - \frac{\phi_s}{\phi_m}\right)\phi_s\frac{\mu}{\mu_f}$$

For the fluid phase, we keep $c_{1f} = 1$ and $c_{2f} = c_{3f} = 0$.

We observe on fig. 5.28 that the increase of the particle velocity is indeed faster closer to the wall. The blunting of the velocity profile is less marked than with the true slip condition. For example, for $\bar{\phi}_s = 0.5$, we are above 0.8 $u_{max}$ at the center in apparent slip and below for true slip.

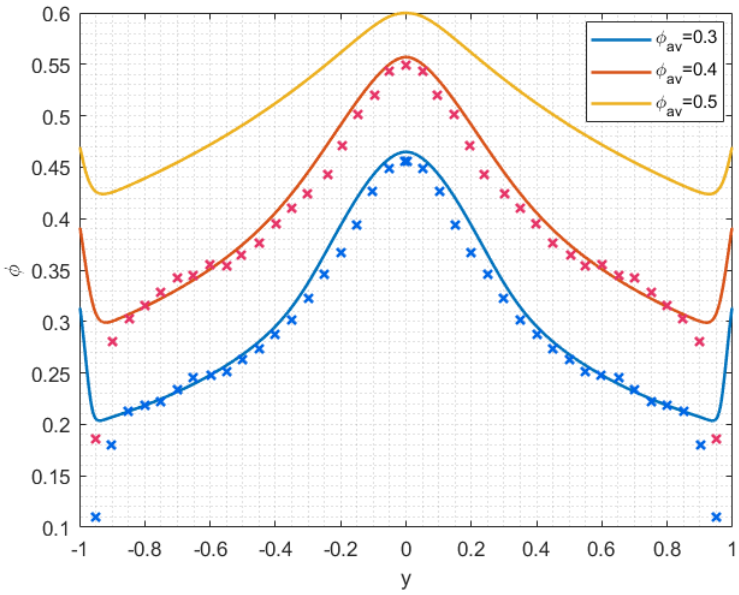


Figure 5.27: Apparent slip - $\phi_s$ profile is very similar to true slip - $l_{ref} = 20\mu m$,$u_{max} = 200\mu m/s$

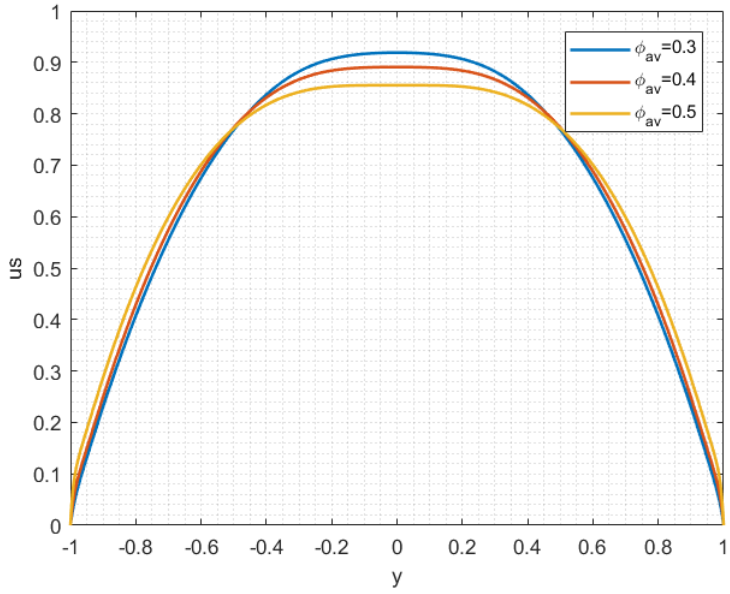


Figure 5.28: Apparent wall slip is closer to no slip condition- the increase of velocity at the wall is sharper especially for higher $\bar{\phi}_s$

## 5.3 Vertical channels - Gravity driven flows

The second part of this analysis is dedicated to gravity driven flows. The idea is to take advantage of the gravity in order to benefit from a completely passive filtration method. There would then be no need to have a pump driving the suspension. It will be however impossible to tailor the flow with a pressure gradient in order to modify the velocity $u_{max}$ since the gravity forcing term will always be constant. The two parameters we will analyse are the channel height and the average volume fraction.

### 5.3.1 Impact of the channel height

To proceed, we first analyse the volume fraction profile with varying $l_{ref}$. Since the forcing term, the gravity, is constant, the velocity $u_{max}$ is increasing quadratically with wider channels. We experience the same trouble with the drag law, mentioned in 6.2.3, so we applied a shrinking factor $\epsilon$ again to $\delta$.
We observe that wider channels have three advantages; the geometry, the particle migration and an higher velocity. Indeed, firstly, wider channels will automatically induce higher mass-flows. Secondly, particle migration is seen to be enhanced for channels with higher $l_{ref}$, see fig 5.29. Also, we can gain nearly two order of magnitude for $u_{max}$ by multiplying the channel height by a factor 8. An increase of $l_{ref}$ is thus very beneficial to the massflow of collected particles. However, we have also to keep in mind that the dynamics to achieve steady state is much faster for smaller confinement ratio ($l_{ref}/D$).[13] Indeed, it would take more time for the flows to develop in wider channels and this would induce a need for longer channels. A trade-off has to be determined. We insist that we are still in the viscous limit ($Re_4 = 2e^{-3}$)

| Case | $l_{ref}[m]$ | $\bar{\phi}_s$ | $\epsilon$ | $u_{max}[m/s]$ |
|---|---|---|---|---|
| 1 | $2e^{-5}$ | 0.3 | 1 | $6.46e^{-6}$ |
| 2 | $4e^{-5}$ | 0.3 | 1 | $2.76e^{-5}$ |
| 3 | $8e^{-5}$ | 0.3 | 0.4 | $1.16e^{-4}$ |
| 4 | $1.6e^{-4}$ | 0.3 | 0.05 | $4.8e^{-4}$ |

| Case | $l_{ref}$ [m] | $\bar{\phi}_s$ | $\epsilon$ | $u_{max}$ [m/s] |
|---|---|---|---|---|
| 5 | $2e^{-5}$ | 0.4 | 1 | $4.03e^{-6}$ |
| 6 | $4e^{-5}$ | 0.4 | 1 | $1.78e^{-5}$ |
| 7 | $8e^{-5}$ | 0.4 | 0.2 | $7.56e^{-5}$ |
| 8 | $1.6e^{-4}$ | 0.4 | 0.05 | $3.11e^{-4}$ |

| Case | $l_{ref}[m]$ | $\bar{\phi}_s$ | $\epsilon$ | $u_{max}[m/s]$ |
|---|---|---|---|---|
| 9 | $2e^{-5}$ | 0.5 | 1 | $1.86e^{-6}$ |
| 10 | $4e^{-5}$ | 0.5 | 0.5 | $8.45^{-6}$ |
| 11 | $8e^{-5}$ | 0.5 | 0.1 | $3.51e^{-5}$ |
| 12 | $1.6e^{-4}$ | 0.5 | 0.03 | $3.2e^{-5}$ |

Table 5.7: 12 different cases, varying $\bar{\phi}_s$ and $l_{ref}$

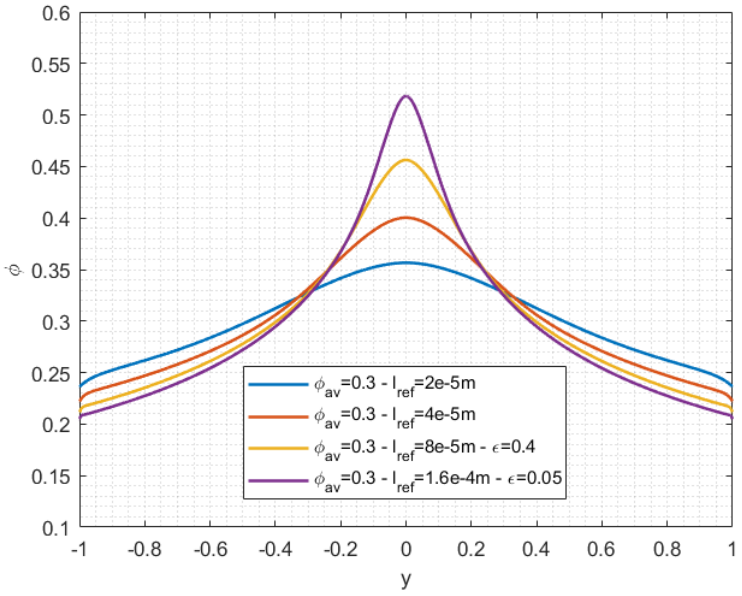


Figure 5.29: Volume fraction profile with gravity driven flows with varying $l_{ref}$ at $\bar{\phi}_s = 0.3$ - Particle migration is enhanced for higher channels up until $\phi_s = 0.52$

### Analysis of the stresses

The enhanced particle migration for higher $l_{ref}$ can be analysed thanks to the different stresses in the the momentum balance along y. As shown on fig 5.30, the granular pressure is reaching 12% of the product F $l_{ref}$ at the center when

$l_{ref}$ is 20 $\mu m$. This explains the higher resistance of particles at the center to be compacted. There is an higher accumulation of particles when the channel is wider as the granular pressure is halved proportionally to the product F $l_{ref}$ when $l_{ref}$ is $1.6e^{-4}m$. The non-uniformity of the normal viscous stresses is also observed. They decrease way faster along y with smaller channels. In fact, the granular pressure is increasing for smaller channels because of the predominance of the intergranular stresses as seen on fig. 5.31. They even represent 20% of the product $l_{ref}$ F when $l_{ref}$ is 20 microns. We also see that the balance between the diffusion term and the intergranular remain constant. The ratio between each other is balanced. However, the decrease of $l_{ref}$ increases the ratio of the granular pressure to the F $l_{ref}$ product. This then leads to a decrease of the volume fraction for the variation along y of the viscous stresses and the term $p_s$ $\phi_s$ to be balanced.

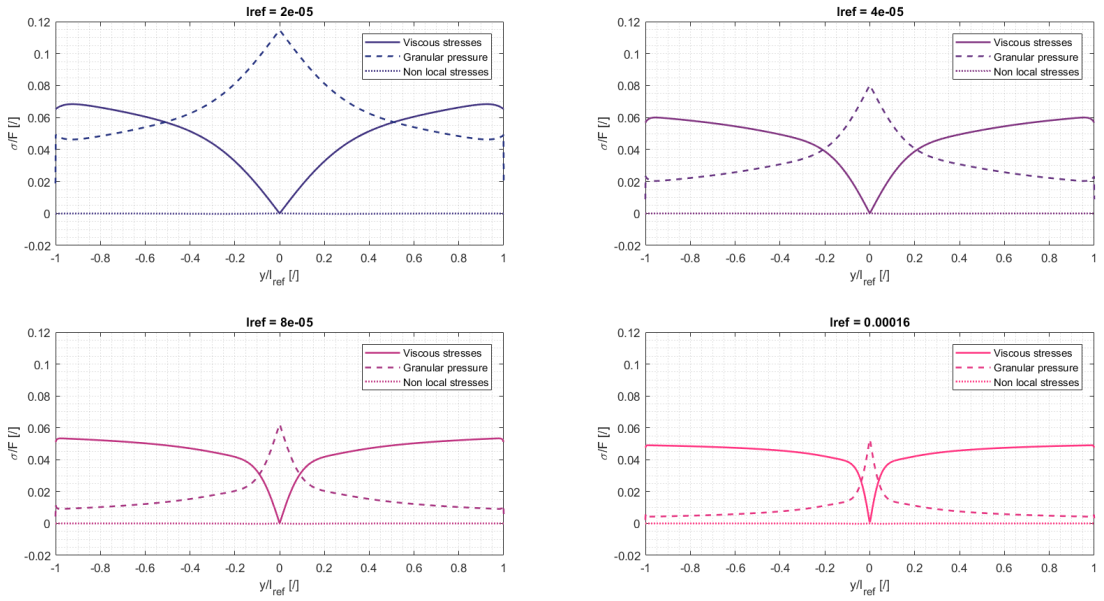


Figure 5.30: Balance of the stresses in the momentum equation for varying $l_{ref}$ at $\bar{\phi}_s = 0.3$ - constant F

Then, we analyse the balance of stresses along x. In the case of vertical channels, I had to ponderate the viscous stresses by the ratio $\frac{\rho_f g \phi_f(y) + \rho_s g \phi_s(y)}{\rho_f g \bar{\phi}_f + \rho_s g \bar{\phi}_s}$, since the forcing term is not constant along y and depends of the volume fraction at this point.
We observe that most of the pressure gradient is dissipated by the granular phase

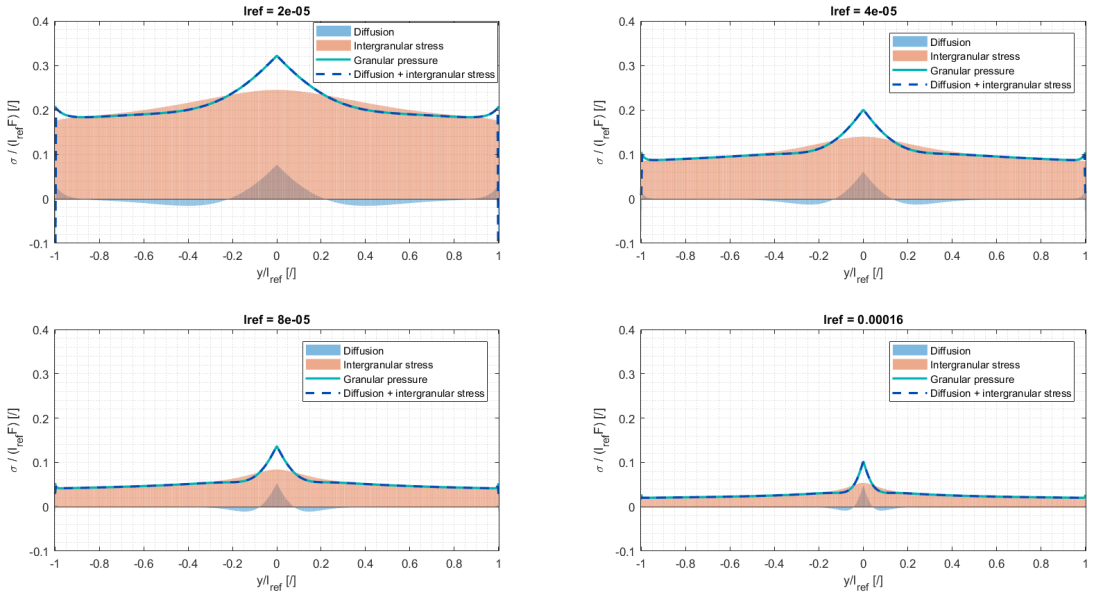


Figure 5.31: Balance of the terms in the compaction equation for varying $l_{ref}$ at $\bar{\phi}_s = 0.3$ - constant F

at the center, this is even more marked for larger channels. At the wall however, 60% of the viscous dissipation is due to the fluid.

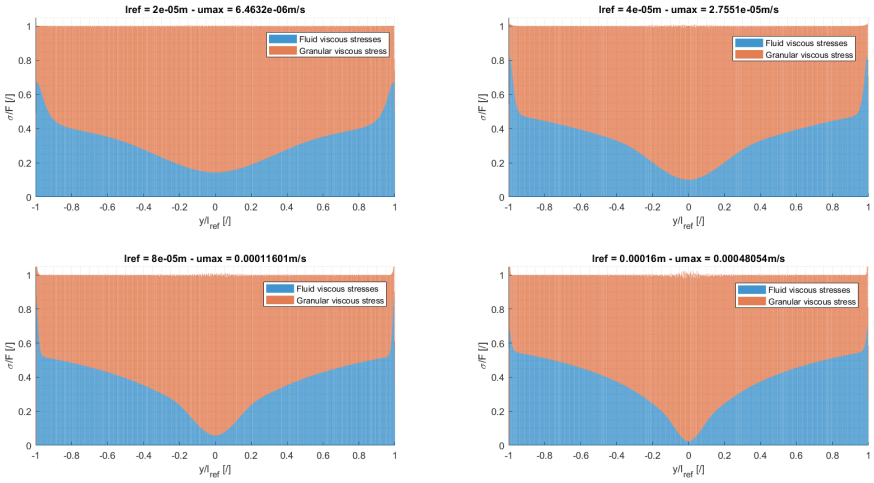


Figure 5.32: Balance of the viscous stresses in gravity driven flows with varying $l_{ref}$ - $\bar{\phi}_s = 0.3$

### Analysis of the mass-flow coefficients

In this section, we compare the mass-flows of particles we are able to extract at the center for different channel half heights $l_{ref}$ and average volume fraction $\bar{\phi}_s$ while using gravity as forcing term. We compare two different mass-flows; the mass-flow of particles if we separate the channel at 50% of the half-height $l_{ref}$ on both sides and the second if we separate at 25%. In the first case, the region where we are harvesting the particles is then the same size as the region where we are not harvesting. In the second case, the harvesting zone is three times smaller than the remaining, unharvested zone. If we want to have an harvesting zone equals to the top and bottom zones (2 times smaller than the remaining zone), we would have to separate at a value of 33% of $l_{ref}$. There is a trade-off when choosing the size of the separation channel. Indeed, to harvest the maximum of particles, we want to increase the height of the separation channel. However, a too big increase would be useless since the average filtrated volume fraction of particles will decrease. We then compare the obtained particle mass-flows in the separation channel ($\dot{Q}_{s-0.5l_{ref}}$ and $\dot{Q}_{s-0.25l_{ref}}$) with the bulk mass flow of particles in the main channel $\dot{Q}_{s-l_{ref}}$. These three massflows are expressed in kg/m s since they also depend on the channel's width. The formula used to calculate the massflows are:

$$\dot{Q}_{s-l_{ref}} = \bar{\phi}_s \rho_s \bar{\tilde{u}}_s u_{max} 2l_{ref} \approx \bar{\phi}_s \rho_s \frac{4}{3} u_{max} l_{ref} [kg/ms] \tag{5.2}$$

$$\dot{Q}_{s-0.5l_{ref}} = \bar{\phi}_{s-0.5l_{ref}} \rho_s \bar{\tilde{u}}_{s-0.5l_{ref}} u_{max} (2l_{ref} 0.5)[kg/ms] \tag{5.3}$$

$$\dot{Q}_{s-0.25l_{ref}} = \bar{\phi}_{s-0.25l_{ref}} \rho_s \bar{\tilde{u}}_{s-0.25l_{ref}} u_{max} (2l_{ref} 0.25)[kg/ms] \tag{5.4}$$

**$\bar{\phi}_s$ = 0.3**

| $l_{ref}[m]$ | $u_{max}[m/s]$ | $\dot{Q}_{s-l_{ref}}$ [kg/m s] | $\dot{Q}_{s-0.5l_{ref}}$ | $\dot{Q}_{s-0.25l_{ref}}$ |
|---|---|---|---|---|
| $2e^{-5}$ | $6.46e^{-6}$ | $1.1e^{-7}$ | $8.05e^{-8} - 73.9\%$ | $4.42e^{-8} - 40.7\%$ |
| $4e^{-5}$ | $2.76e^{-5}$ | $9.3e^{-7}$ | $7.1e^{-7} - 77\%$ | $4.1e^{-7} - 44\%$ |
| $8e^{-5}$ | $1.16e^{-4}$ | $7.79e^{-6}$ | $6.2e^{-6} - 79\%$ | $3.68e^{-6} - 47\%$ |
| $1.6e^{-4}$ | $4.8e^{-4}$ | $6.454e^{-5}$ | $5.24e^{-5} - 81\%$ | $3.18e^{-5} - 49\%$ |

$\bar{\phi}_s$ **= 0.4**

| $l_{ref}[m]$ | $u_{max}[m/s]$ | $\dot{Q}_{s-l_{ref}}$ [kg/m s] | $\dot{Q}_{s-0.5l_{ref}}$ | $\dot{Q}_{s-0.25l_{ref}}$ |
|---|---|---|---|---|
| $2e^{-5}$ | $4.03e^{-6}$ | $9e^{-8}$ | $6.44e^{-8} - 71\%$ | $3.45e^{-8} - 38.2\%$ |
| $4e^{-5}$ | $1.78e^{-5}$ | $8e^{-7}$ | $5.9e^{-7} - 74\%$ | $3.3e^{-7} - 40.7\%$ |
| $8e^{-5}$ | $7.56e^{-5}$ | $6.7e^{-6}$ | $5.13e^{-6} - 75.7\%$ | $2.92e^{-6} - 43\%$ |
| $1.6e^{-4}$ | $3.11e^{-4}$ | $5.56e^{-5}$ | $4.27e^{-5} - 76.5\%$ | $2.45e^{-5} - 44\%$ |

$\bar{\phi}_s$ **= 0.5**

| $l_{ref}[m]$ | $u_{max}[m/s]$ | $\dot{Q}_{s-l_{ref}}$ [kg/m s] | $\dot{Q}_{s-0.5l_{ref}}$ | $\dot{Q}_{s-0.25l_{ref}}$ |
|---|---|---|---|---|
| $2e^{-5}$ | $1.86e^{-6}$ | $5e^{-8}$ | $3.56e^{-8} - 68\%$ | $1.87e^{-8} - 35.7\%$ |
| $4e^{-5}$ | $8.45^{-6}$ | $4.7e^{-7}$ | $3.3e^{-7} - 69.5\%$ | $1.8e^{-7} - 37\%$ |
| $8e^{-5}$ | $3.51e^{-5}$ | $3.93e^{-6}$ | $2.76e^{-6} - 70.2\%$ | $1.49e^{-6} - 37.7\%$ |
| $1.6e^{-4}$ | $1.42e^{-4}$ | $3.2e^{-5}$ | $2.24e^{-5} - 70.3\%$ | $1.2e^{-5} - 37.8\%$ |

An increase of the channel half-height $l_{ref}$ has shown to enhance particle migration, see fig 5.29. This can be deducted from the mass-flow coefficients. Indeed, when we increase $l_{ref}$ from 20 to 160 microns, $Q_{s-0.5l_{ref}}$ and $Q_{s-0.5l_{ref}}$ are increased. When $\bar{\phi}_s = 0.3$, we can gain 7% for $Q_{s-0.5l_{ref}}$ and nearly 9 % for $Q_{s-0.25l_{ref}}$. The percentage of harvested particles is always increasing with the channel's height. We then have interest to increase it.

The mass-flow of particles if we separate the channel at 25% of the channel height is more than the half of the mass-flow at a separation of 50% of the channel height. Indeed, since the particles are accumulating at the center, an increase of the harvesting zone decreases the average harvested particle concentration. By separating at $l_{ref} = 25\%$ on both sides, we are able to collect 50% of the particles initially present in the channel when $l_{ref} = 160\mu m$ and $\bar{\phi}_s = 0.3$.

### 5.3.2 Impact of the average volume fraction

The particle volume fraction in gravity driven flows tends to be smoother compared to pressure driven flows, as seen on fig. 5.33. We could nearly say that there is an offset of $\delta\bar{\phi}_s$ between each one of them, which was not true in pressure driven flows.

#### Analysis of the stresses

It is globally due to the fact that the compaction equation is majored by intergranular stresses. The diffusion term plays a role only when $\bar{\phi}_s$ reaches 0.4-0.5, see the blue terms in fig. 5.34. This can be seen on fig. 5.33, where the central volume fraction of the yellow and purple curves is a bit flattened as the averaged volume fraction increases. We also calculated the stresses in the momentum balance and noticed that in the momentum balance when $\bar{\phi}_s = 0.2$, the two terms are really small. This explains the low particle migration of the blue curve on fig. 5.33 that only reaches $\phi_s = 0.25$. As the averaged volume fraction is increased, both the viscous terms and $p_s\ \phi_s$ are increasing.

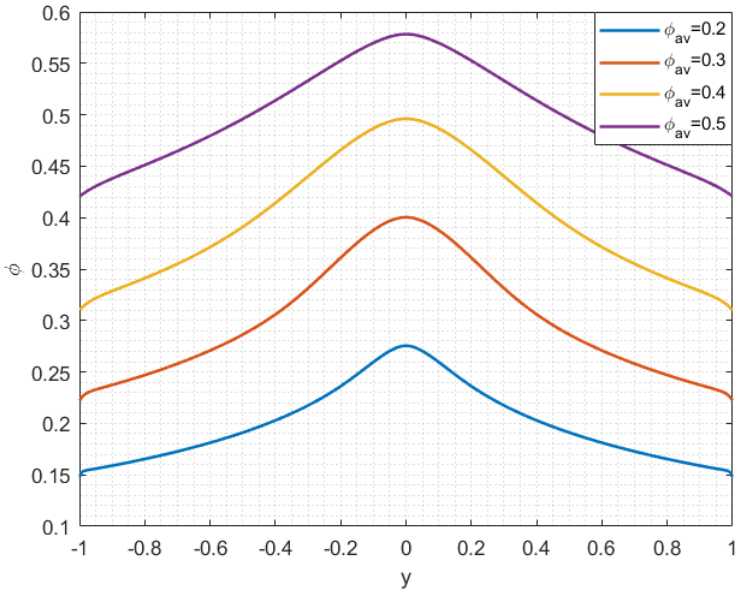


Figure 5.33: Particle volume fraction with varying $\bar{\phi}_s$ gravity driven flows at $l_{ref} = 40\mu m$

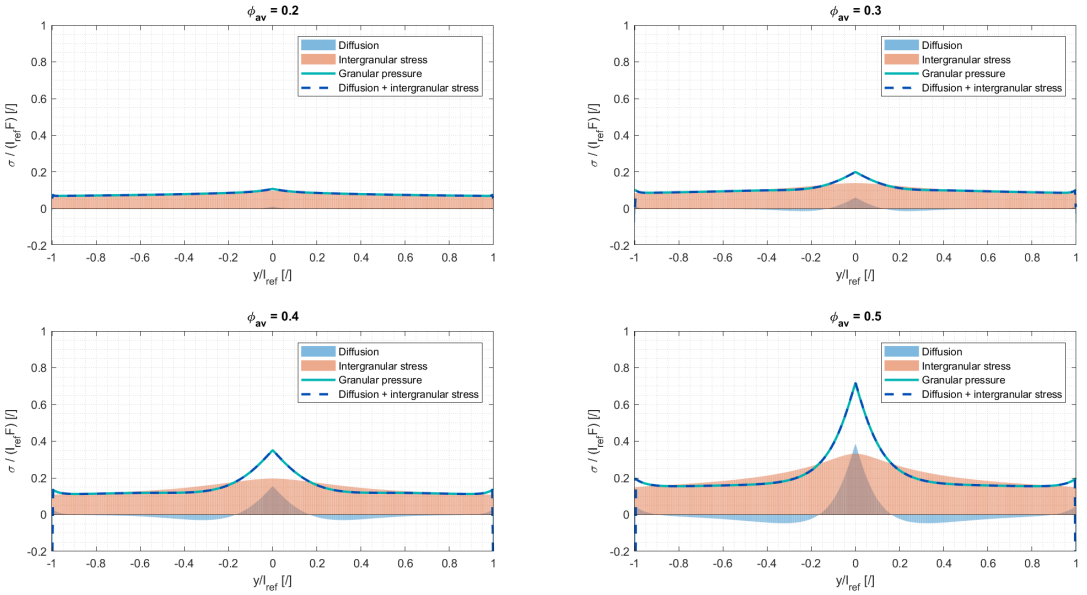


Figure 5.34: Balance of the terms in the compaction equation for varying $\bar{\phi}_s$ gravity driven flows at $l_{ref} = 40\mu m$

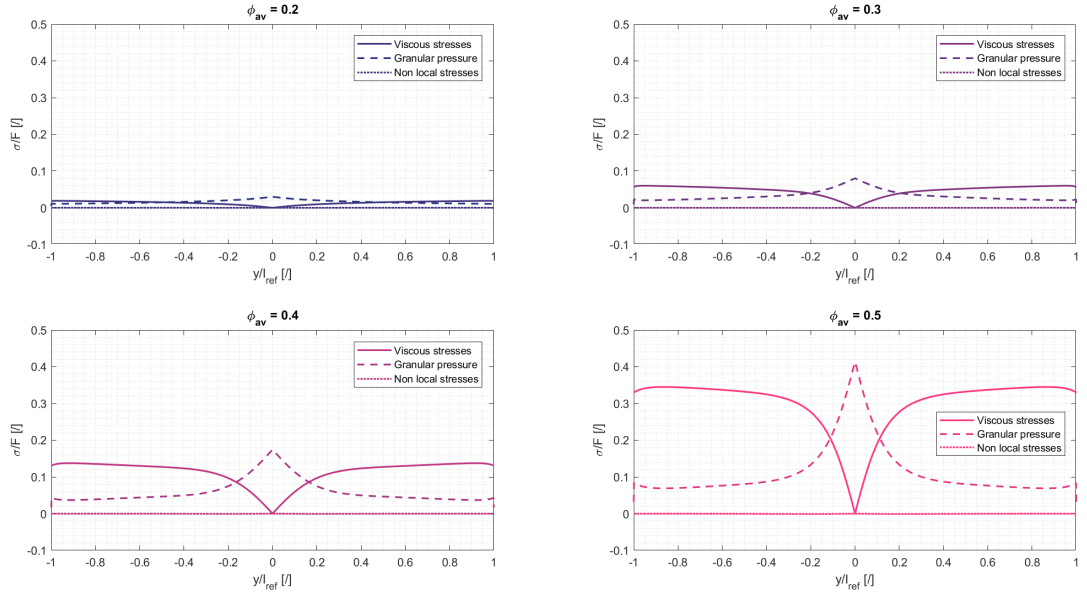


Figure 5.35: Balance of the stresses in the momentum equation for varying $\bar{\phi}_s$ gravity driven flows at $l_{ref} = 40\mu m$

**Analysis of the mass-flow coefficients**

One major impact we observe is that in order to maximise the collected particles mass-flow, we do not have to increase the entering average volume fraction, quite the contrary! Indeed, when the entering suspensions are denser, the viscosity is increasing and the flow is slowed down since the forcing term is constant, with leads to a negative impact on the mass-flow. For example, between $\bar{\phi}_s = 0.5$ and $\bar{\phi}_s = 0.3$, we can except more than a doubling of the mass-flow of particles. This is natural since the velocity at the center is more than tripled with the lowest averaged volume fraction (going from $u_{max} = 1.86e^{-6}$ to $6.46e^{-6}$ m/s at $l_{ref} = 2e^{-5}m$) What we also observe is that in denser suspensions, the increase of the mass-flow coefficients with $l_{ref}$ is slower. Gaining 7 and 9 % for the two mass-flow coefficients at $\bar{\phi}_s = 0.3$, we are only gaining 5.5 - 5.8 % for $\bar{\phi}_s = 0.4$ and 2.3 - 2.1 % when $\bar{\phi}_s = 0.5$. There is thus a clear incentive to start with less dense suspensions. This corroborates with the results from Husband et al. in 1994 [16]. The best way to harvest particles from a dense suspension in gravity driven flow would then involve an average volume fraction around $\bar{\phi}_s = 0.3$ and with a channel half-height of 160 microns for the case studied (D = 1 $\mu m$).

## 5.4 Comparison with dry granular media

In this section, we will compare the flow of a dense suspension in a vertical channel with the flow of dense dry granular media. In short, we will change the properties of the fluid where the particles are suspended, replace it by air's and analyse the impact it will have on the flow. To do so, we fix a new value for the fluid viscosity $\mu_f$ and the density $\rho_f$.

| Parameters | Original value | Unit |
|---|---|---|
| $\mu_f$ | $1.8e^{-5}$ | Pa s |
| $\rho_f$ | 1.225 | kg/m$^3$ |

Table 5.8: Modified physical parameters

### 5.4.1 Impact of the channel height

We observe that the volume fraction reaches similar but smaller values than in the case where the fluid was a mixture of water and glycerin. Compared to gravity driven suspension, the volume fraction is on average between 0.03 - 0.05 smaller at the center. This is more marked for larger channels. From $\phi_{max} = 0.52$ at the center when $l_{ref} = 160\mu m$ in the suspension, we reach 0.47 for the dry granular media.

| $l_{ref}$ [m] | $\bar{\phi_s}$ | $\epsilon$ | $u_{max}$ [m/s] | $F = \rho_s \bar{\phi_s} g[Pa/m]$ |
|---|---|---|---|---|
| $2e^{-5}$ | 0.3 | 1 | $5.87e^{-3}$ | $-6.19e^3$ |
| $4e^{-5}$ | 0.3 | 1 | $2.5e^{-2}$ | $-6.19e^3$ |
| $8e^{-5}$ | 0.3 | 0.4 | $1.06e^{-1}$ | $-6.19e^3$ |
| $1.6e^{-4}$ | 0.3 | 0.1 | $4.48e^{-1}$ | $-6.19e^3$ |

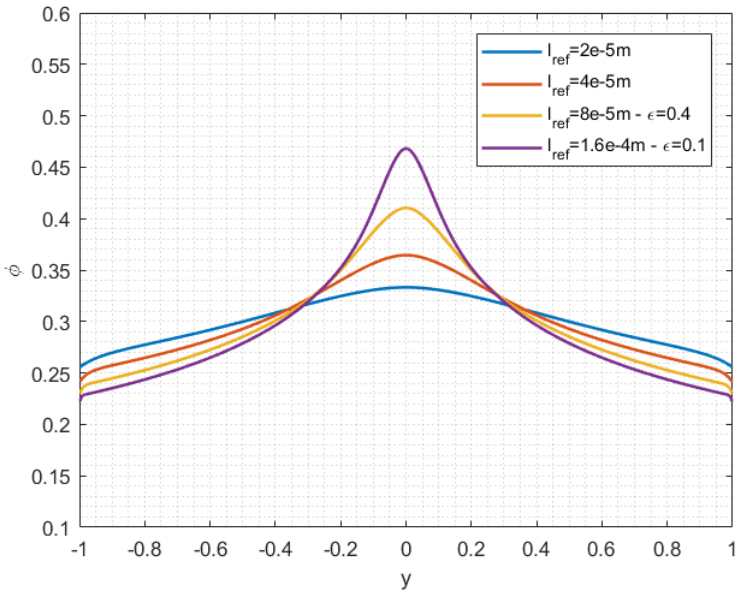


Figure 5.36: Volume fraction profile when the fluid is air

### 5.4.2 Analysis of the stresses

#### Along x

Since $\rho_f$ is smaller by 3 orders of magnitude, we except that the fluid phase will be controlled mainly by the drag instead of the gravity forcing term ($\rho_f g \phi_f$ small compared to $\delta(u_f - u_s)$) in equ. 3.6. The main equation is thus the balance of momentum of the granular phase, equ. 3.7 and we can suppose that F $\approx \rho_s \phi_s g$. The air will be driven by the drag with the granular phase and the value of the drag will be equal to the fluid viscous stresses, in blue on fig 5.37.
We observe that the granular viscous stresses along x are everywhere bigger than the fluid's, except at the wall where they are equal. At the center, the fluid viscous stresses are approaching zero as $l_{ref}$ increases. If there were no drag between the two phases, the air velocity would be zero everywhere and the dissipation will be due solely to the granular viscous stresses.
Since the fluid viscosity is also drastically decreased in this case (from $4e^{-2}$ to $1.8e^{-5}$ Pa s), the velocities of both the granular and fluid phase are drastically increasing. This will be further analysed in the section dedicated to the mass-flow.

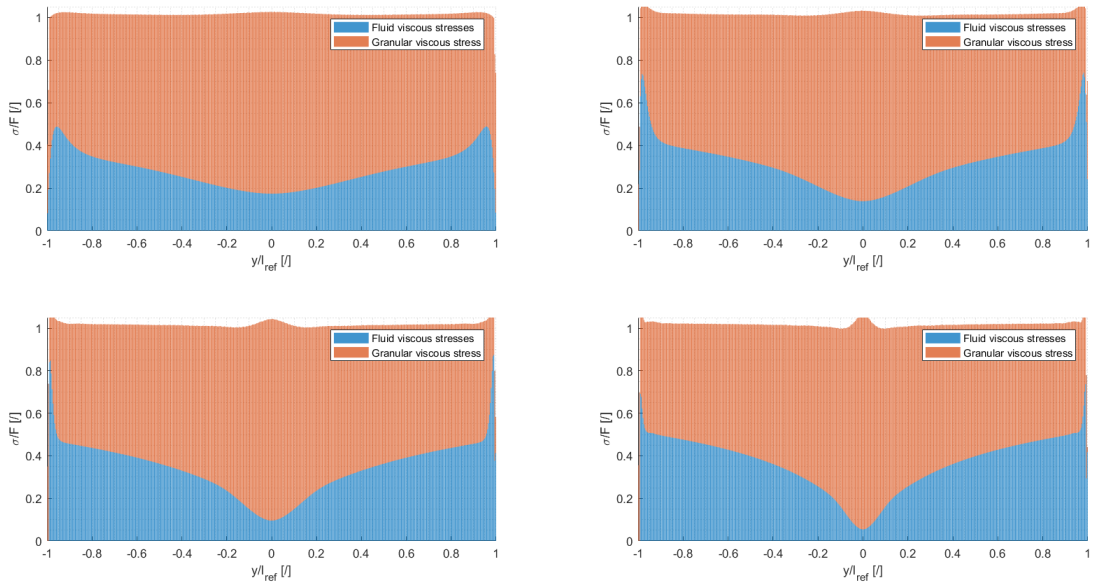


Figure 5.37: Balance between granular and fluid viscous stresses along x - $\bar{\phi}_s = 0.3$

### Along y

Concerning the momentum balance along y, it is very similar to the gravity driven suspension. It is normal since it only concerns the granular phase. However, the relative value of these stresses is doubled everywhere. This increase of relative importance of both the diffusion term and the intergranular stress is due to the fact that the forcing term is decreasing since $\rho_f$ is negligible. When we had an average forcing term equal to $g(\bar{\phi}_s\rho_s + \phi_f\rho_f) = 1.4e^4 Pa/m$ when $\bar{\phi}_s = 0.3$, we now have only $g\bar{\phi}_s\rho_s = 6.19e^3 Pa/m$. This is true for both the compaction equation and the momentum balance along y, see fig. 5.38 & 5.39.

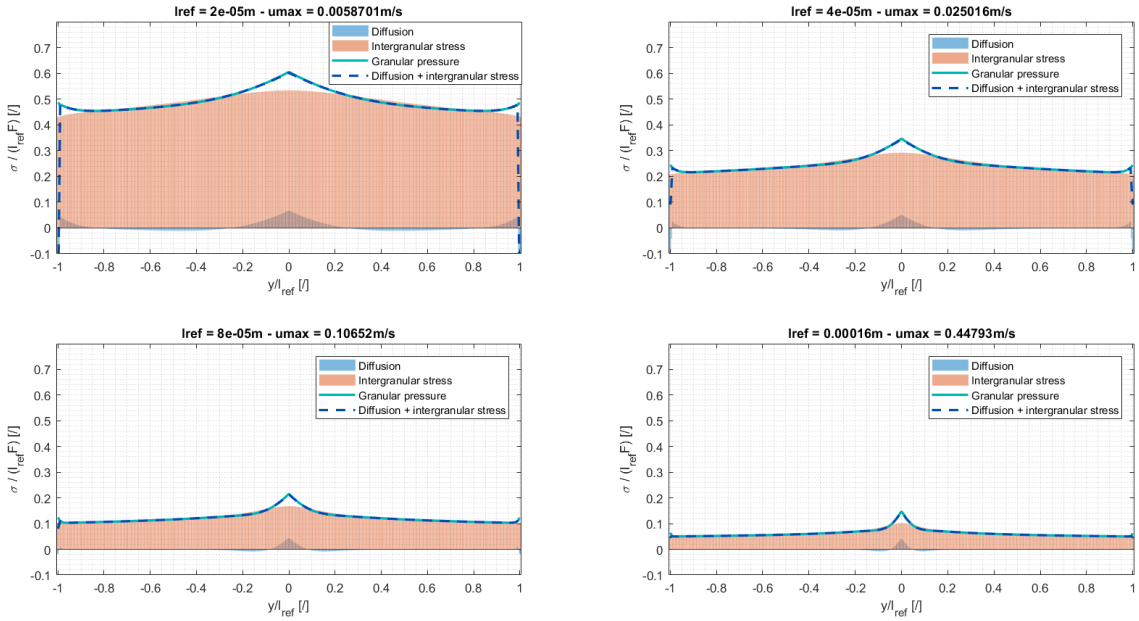


Figure 5.38: Stresses balance in the compaction equation - $\bar{\phi}_s = 0.3$

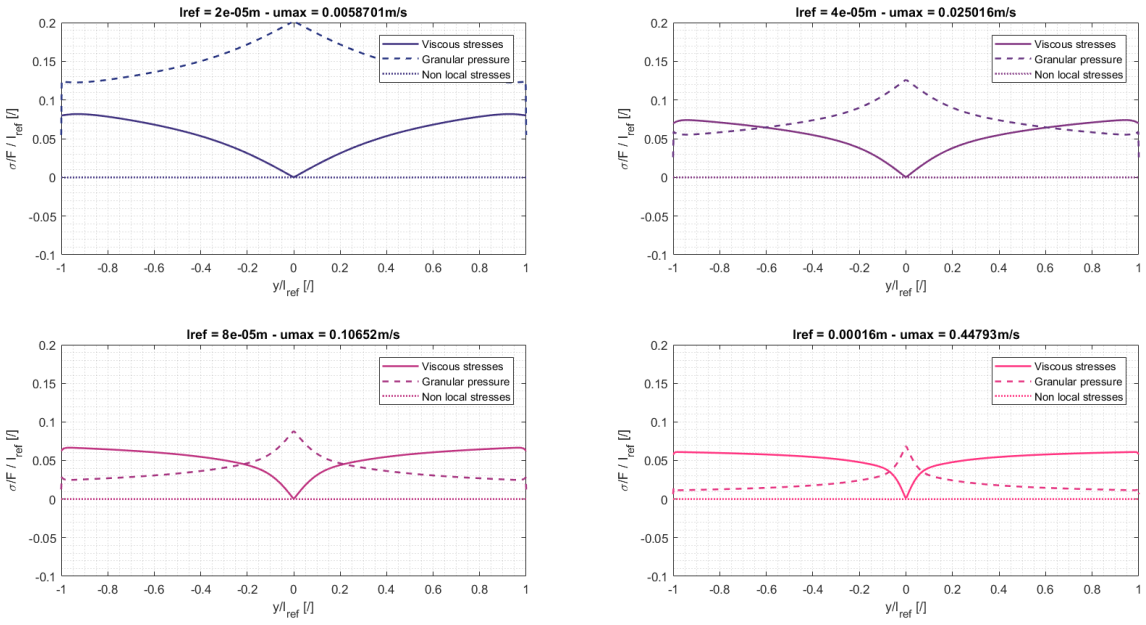


Figure 5.39: Stresses balance of the momentum along y - $\bar{\phi}_s = 0.3$

### 5.4.3 Analysis of the mass-flow coefficients

When we compare the mass-flow coefficients on table 5.9, we have an average loss of 3% of the collected particles mass-flow compare to the total mass-flow. However, we notice that since the viscosity of the fluid is way smaller, the velocity is higher. We then gain 3 orders of magnitude for the general mass-flow.

$\bar{\phi}_s$ **= 0.3**

| $l_{ref}[m]$ | $u_{max}[m/s]$ | $\dot{Q}_{s-l_{ref}}$ [kg/m s] | $\dot{Q}_{s-0.5l_{ref}}$ | $\dot{Q}_{s-0.25l_{ref}}$ |
|---|---|---|---|---|
| $2e^{-5}$ | $5.87e^{-3}$ | $1e^{-4}$ | $7e^{-5} - 71.7\%$ | $4e^{-5} - 38.1\%$ |
| $4e^{-5}$ | $2.5e^{-2}$ | $8.4e^{-4}$ | $6.2e^{-4} - 74.2\%$ | $3.4e^{-4} - 40.7\%$ |
| $8e^{-5}$ | $1.06e^{-1}$ | $7.15e^{-3}$ | $5.5e^{-3} - 76.7\%$ | $3.13e^{-3} - 43.6\%$ |
| $1.6e^{-4}$ | $1.59e^{-1}$ | $6.01e^{-2}$ | $4.7e^{-2} - 78.7\%$ | $2.78e^{-2} - 46.1\%$ |

Table 5.9: Mass-flow coefficients for dry granular media in vertical channels

# 6 Conclusion

In this master thesis, we carried out a numerical study on the shear-induced particle migration in dense non-colloidal suspensions flowing in confined micro-channels at low Reynolds number. The end goal was to evaluate the feasibility of a particle harvesting system taking advantage of this phenomenon.

First of all, we analysed the impact of the two physical parameters $\beta_0$ and $\gamma_0$ that controls the amplitude of the intergranular and non-local stresses. They are both seen to inhibit particle migration by increasing the granular pressure at the center.

Then, we studied pressure driven flows in horizontal channels and gravity driven flows in vertical channels. We analysed the effect of the average volume fraction, the pressure gradient and the channel height. We defined the impact of the boundary conditions by applying no-slip, true slip and apparent slip conditions at the wall. We also studied the drag law and the impact of the number of grid points.
In the horizontal channels, an increase of the channel height while keeping the velocity constant is induced by a lower pressure gradient and does not improve particle migration. However, increasing the pressure gradient in a constant channel height is increasing particle concentration at the center. We thus have interest to increase the pressure gradient to enhance the velocity for a defined channel height. However, we must remain in the viscous regime, the Re must remain below 1. It induces that the product $u_{max}\ l_{ref}$ must be sufficiently smaller than $\frac{\mu_f}{\rho_f}$. We are also limited with $l_{ref}$ by the confinement ratio $\frac{2l_{ref}}{D}$. Indeed, particle migration is if the channel height is too big,

In the vertical channels, the forcing term is constant and depends on the density of the two phases. As the channel height increases, particle migration is enhanced. We can except an harvesting of 50% of the particles in a collecting channel having half of the total height when $\bar{\phi}_s = 0.3$ and $l_{ref} = 160\mu m$. For both vertical and horizontal channels, our mass-flow coefficients analysis concludes that it is not very beneficial to increase $\bar{\phi}_s$ above 0.3. Indeed, the granular viscous stresses drastically increase at the expense of the suspension mass-flow.
The last part of this thesis has been dedicated to a parallel analysis where the mixture of glycerine and water is replaced by air in order to see if our model is suitable for granular media. The obtained results conclude that particle migration is a bit diminished but the massflow is increased due to the smaller viscosity of the fluid.

Further analysis could be led by studying bidisperisity or polydispersity of the particles, as it is done by J.F. Morris in 2018 [37]. Indeed, in the industry, the flows we want to filtrate do not always have particles of the same size. Also, it is known that the jamming transition is happening at higher $\bar{\phi}_{s-tot}$ since smaller particles can intercalate between the bigger ones. Bidispersity is also lowering the apparent viscosity of the suspension.[14]

# A

# Derivation of the governing equations

- $\tilde{\rho} = \frac{\rho}{\rho_{ref}} \leftrightarrow \tilde{\rho_f} = \frac{\rho_f}{\rho_f} = 1$ and $\tilde{\rho_s} = \frac{\rho_s}{\rho_f}$
- $\tilde{\mu} = \frac{\mu}{\mu_{ref}} \leftrightarrow \tilde{\mu_f} = \frac{\mu_f}{\mu_f} = 1$ and $\tilde{\mu_s} = \frac{\mu_s}{\mu_f}$
- $\tilde{u} = \frac{u}{u_{ref}}$
- $\tilde{t} = \frac{t}{t_{ref}}$ where $t_{ref} = \frac{l_{ref}}{u_{ref}}$
- $\tilde{g} = g\frac{t_{ref}}{u_{ref}} = g\frac{l_{ref}}{u_{ref}^2}$
- $\frac{d}{d\tilde{t}} = t_{ref}\frac{d}{dt}$
- $\frac{d\tilde{u}}{d\tilde{x}} = \frac{du}{dx}\frac{l_{ref}}{u_{ref}}$
- $\chi_a = \sqrt{2}\mu_n\left(2\sqrt{\mathbf{V}_s^d : \mathbf{V}_s^d} - \frac{3}{2}\frac{\mathbf{V}_s^d : \mathbf{V}_s^d}{\sqrt{\mathbf{V}_s : \mathbf{V}_s}}\right)$
- $\chi_b = -\frac{\sqrt{2}\mu_n}{\sqrt{\mathbf{V}_s : \mathbf{V}_s}}$
- $\tilde{\chi_a} = \frac{\chi_a \cdot l_{ref}}{\mu_{ref} \cdot u_{ref}}$ and $\tilde{\chi_b} = \frac{\chi_b \cdot u_{ref}}{\mu_{ref} \cdot l_{ref}}$ from Equ (8) & (9) from [34].
- $\tilde{C_s} = \frac{C_s}{\rho_{ref} u_{ref}^2}$ since $C_s = \gamma_s \nabla\phi_s \times \nabla\phi_s [N/m^2]$ and $\tilde{\gamma_0} = \frac{\gamma_0}{\rho_{ref} u_{ref}^2 l_{ref}^2}$

**Fluid phase**

**Dimensional equations**

These two equations are taken from [33] p.426 (4.1 & 4.2). The pressure gradient term is replaced by the gravity term.

$$\frac{d(\rho_f \phi_f)}{d_f t} + \rho_f \phi_f \nabla \cdot u_f = 0 \tag{A.1}$$

$$\rho_f \phi_f \frac{du_f}{d_f t} = \nabla \cdot ((\zeta_f \nabla \cdot u_f)\phi_f I + 2\mu_f \phi_f V_f^d) - (\delta(u_f - u_s) + p_f \nabla \phi_s) + g\rho_f \phi_f \tag{A.2}$$

**Non-dimensional equation for the momentum**

$$\rho_{ref}\phi_f \left( \frac{d(\tilde{u_f} u_{ref})}{d(\tilde{t} \cdot t_{ref})} + \frac{u_{ref}\tilde{u_f}}{l_{ref}} \cdot \tilde{\nabla}(u_{ref}\tilde{u_f}) \right) = \frac{1}{l_{ref}} \tilde{\nabla} \cdot \left( (\tilde{\zeta_f} \frac{\mu_{ref}}{l_{ref}} \tilde{\nabla} \cdot (\tilde{u_f} u_{ref}))\phi_f I + 2\mu_{ref}\phi_f \frac{u_{ref}}{l_{ref}} \tilde{V_f^d} \right)$$
$$- (\delta(\tilde{u_f} u_{ref} - \tilde{u_s} u_{ref}) + \frac{\tilde{p_f} \rho_{ref} u_{ref}^2}{l_{ref}} \tilde{\nabla} \phi_s) + \frac{\tilde{g} \rho_{ref} \phi_f u_{ref}^2}{l_{ref}}$$

We then multiply both sides of the equation by a factor $\frac{l_{ref}}{\rho_{ref} u_{ref}^2}$.

$$\phi_f \left( \frac{d\tilde{u_f}}{d\tilde{t}} + \tilde{u_f} \cdot \tilde{\nabla} \tilde{u_f} \right) = \frac{\mu_{ref}}{\rho_{ref} l_{ref} u_{ref}} \tilde{\nabla} \cdot \left( (\tilde{\zeta_f} \tilde{\nabla} \cdot \tilde{u_f})\phi_f I + 2\phi_f \tilde{V_f^d} \right) - (\delta(\tilde{u_f} - \tilde{u_s}) + \tilde{p_f} \tilde{\nabla} \phi_s) + \tilde{g}\phi_f$$

$$\phi_f \left( \frac{d\tilde{u_f}}{d\tilde{t}} + \tilde{u_f} \cdot \tilde{\nabla} \tilde{u_f} \right) = \frac{1}{Re} \tilde{\nabla} \cdot \left( (\tilde{\zeta_f} \tilde{\nabla} \cdot \tilde{u_f})\phi_f I + 2\phi_f \tilde{V_f^d} \right) - (\delta(\tilde{u_f} - \tilde{u_s}) + \tilde{p_f} \tilde{\nabla} \phi_s) + \tilde{g}\phi_f$$

**1D Stationnary Poiseuille flow**

The problem is stationnary, it leads to

$$\frac{d\tilde{u_f}}{d\tilde{t}} = 0$$

Since our problem is unidirectionnal, we assume that

$$u_f = u_f(y)\hat{\mathrm{e}}_x$$

$$\tilde{u_f}(y) \cdot \tilde{\nabla} \tilde{u_f}(y) = \tilde{u_f}(y) \hat{\mathrm{e}}_x \cdot \left( \frac{d\tilde{u_f}(y)}{dx} \hat{\mathrm{e}}_x + \frac{d\tilde{u_f}(y)}{dy} \hat{\mathrm{e}}_y \right) = 0$$

$$\begin{aligned} \frac{1}{Re} \tilde{\nabla} \cdot \left( (\tilde{\zeta_f} \tilde{\nabla} \cdot (\tilde{u_f})) \phi_f I + 2\phi_f \tilde{V_f^d} \right) &= \frac{1}{Re} \tilde{\nabla} \cdot \left( (\tilde{\zeta_f} \left( \frac{d}{dx} \hat{\mathrm{e}}_x + \frac{d}{dy} \hat{\mathrm{e}}_y \right) \cdot (\tilde{u_f}(y) \hat{\mathrm{e}}_x)) \phi_f \delta_{ij} \hat{\mathrm{e}}_x \hat{\mathrm{e}}_y \right. \\ &\quad \left. + 2\phi_f \frac{1}{2} \left( \tilde{\nabla} \tilde{u_f} + \tilde{\nabla} \tilde{u_f}^t \right) \right) \\ &= \frac{1}{Re} \left( \frac{d}{dx} \hat{\mathrm{e}}_x + \frac{d}{dy} \hat{\mathrm{e}}_y \right) \cdot \left( \phi_f \left( \frac{d\tilde{u_f}}{dy} \hat{\mathrm{e}}_x \hat{\mathrm{e}}_y + \frac{d\tilde{u_f}}{dy} \hat{\mathrm{e}}_y \hat{\mathrm{e}}_x \right) \right) \\ &= \frac{1}{Re} \frac{d}{dy} \cdot \left( \phi_f \frac{d\tilde{u_f}(y)}{dy} \right) \hat{\mathrm{e}}_x \end{aligned}$$

and $P_f = p_f(y) - Fx = 0$ since F and $p_f$ =0

$$\tilde{p_f} \tilde{\nabla} \phi_s = \tilde{p_f} \frac{d\phi_s}{dy} \hat{\mathrm{e}}_y = 0$$

We then have our final equation:

$$\boxed{\frac{1}{Re} \frac{d}{dy} \left( (1 - \phi_s) \frac{d\tilde{u_f}(y)}{dy} \right) = \delta(\tilde{u_f} - \tilde{u_s}) - \tilde{g}(1 - \phi_s)}$$

**Granular phase**

**Dimensional equations**

$$\frac{d(\rho_s \phi_s)}{d_s t} + \rho_s \phi_s \nabla \cdot u_s = 0$$

$$\rho_s \phi_s \frac{du_s}{d_s t} = \nabla \cdot ((\zeta_s \nabla \cdot u_s + \chi_a) \phi_s I + 2\mu_s \phi_s V_s^d + \chi_b \phi_s V_s \cdot V_s) - \nabla \cdot C_s + (\delta(u_f - u_s) + p_f \nabla \phi_s) + g \rho_s \phi_s$$

**Non-dimensional equations**

$$\tilde{\rho_s}\rho_{ref}\phi_s\left(\frac{d(\tilde{u_s}u_{ref})}{d(\tilde{t}\cdot t_{ref})}+\frac{u_{ref}\tilde{u_s}}{l_{ref}}\cdot\tilde{\nabla}(u_{ref}\tilde{u_s})\right)$$
$$=\frac{1}{l_{ref}}\tilde{\nabla}\cdot\left((\tilde{\zeta_s}\frac{\mu_{ref}}{l_{ref}}\tilde{\nabla}\cdot(\tilde{u_s}u_{ref})+\tilde{\chi_a}\frac{\mu_{ref}u_{ref}}{l_{ref}})\phi_s I+2\tilde{\mu_s}\mu_{ref}\phi_s\frac{u_{ref}}{l_{ref}}\tilde{V_s^d}+\tilde{\chi_b}\phi_s\frac{\mu_{ref}l_{ref}}{u_{ref}}\cdot\frac{u_{ref}^2}{l_{ref}^2}(\tilde{V_s}*\tilde{V_s})\right)$$
$$-\frac{\rho_{ref}u_{ref}^2}{l_{ref}}\tilde{\nabla}\cdot\tilde{C_s}+(\delta(\tilde{u_f}u_{ref}-\tilde{u_s}u_{ref})+\frac{\tilde{p_f}\rho_{ref}u_{ref}^2}{l_{ref}}\tilde{\nabla}\phi_s)+\frac{\tilde{g}\tilde{\rho_s}\rho_{ref}\phi_s u_{ref}^2}{l_{ref}}$$

We then multiply again both sides of the equation by the factor $\frac{l_{ref}}{\rho_{ref}u_{ref}^2}$.

$$\tilde{\rho_s}\phi_s\left(\frac{d\tilde{u_s}}{d\tilde{t}}+\tilde{u_s}\cdot\tilde{\nabla}\tilde{u_s}\right)=\frac{\mu_{ref}}{\rho_{ref}l_{ref}u_{ref}}\tilde{\nabla}\cdot\Big((\tilde{\zeta_s}\tilde{\nabla}\cdot\tilde{u_s}+\tilde{\chi_a})\phi_s I+2\tilde{\mu_s}\phi_s\tilde{V_s^d}+\tilde{\chi_b}\phi_s(\tilde{V_s}*\tilde{V_s})\Big)-\tilde{\nabla}\cdot\tilde{C_s}$$
$$-(\delta(\tilde{u_f}-\tilde{u_s})+\tilde{p_f}\tilde{\nabla}\phi_s)+\tilde{\rho_s}\tilde{g}\phi_s$$

$$\tilde{\rho_s}\phi_s\left(\frac{d\tilde{u_s}}{d\tilde{t}}+\tilde{u_s}\cdot\tilde{\nabla}\tilde{u_s}\right)=\frac{1}{Re}\tilde{\nabla}\cdot\Big((\tilde{\zeta_s}\tilde{\nabla}\cdot\tilde{u_s}+\tilde{\chi_a})\phi_s I+2\tilde{\mu_s}\phi_s\tilde{V_s^d}+\tilde{\chi_b}\phi_s(\tilde{V_s}*\tilde{V_s})\Big)-\tilde{\nabla}\cdot\tilde{C_s}$$
$$-(\delta(\tilde{u_f}-\tilde{u_s})+\tilde{p_f}\tilde{\nabla}\phi_s)+\tilde{\rho_s}\tilde{g}\phi_s$$

**1D Stationnary Poiseuille flow**

The problem is stationnary, it leads to

$$\frac{d\tilde{u_s}}{d\tilde{t}}=0$$

Since our problem is unidirectionnal, we assume that

$$u_s=u_s(y)\hat{\mathrm{e}}_x$$

$$\tilde{u_s}(y)\cdot\tilde{\nabla}\tilde{u_s}(y)=\frac{d\tilde{u_s}(y)}{dx}\hat{\mathrm{e}}_x+\frac{d\tilde{u_s}(y)}{dy}\hat{\mathrm{e}}_y=\frac{d\tilde{u_s}(y)}{dy}\hat{\mathrm{e}}_y$$

$$\begin{aligned}\frac{1}{Re}\tilde{\nabla}\cdot\left((\tilde{\zeta_s}\tilde{\nabla}\cdot\tilde{u_s}+\chi_a)\phi_s I+2\tilde{\mu_s}\phi_f\tilde{V_s^d}\right) &= \frac{1}{Re}\tilde{\nabla}\cdot\left((\tilde{\zeta_s}\left(\frac{d}{dx}\hat{\mathrm{e}}_x+\frac{d}{dy}\hat{\mathrm{e}}_y\right)\cdot(\tilde{u_s}(y)\hat{\mathrm{e}}_x+\chi_a))\phi_f\delta_{ij}\hat{\mathrm{e}}_x\hat{\mathrm{e}}_y\right.\\ &\quad+2\tilde{\mu_s}\phi_s\frac{1}{2}\left(\tilde{\nabla}\tilde{u_s}+\tilde{\nabla}\tilde{u_s}^t\right)\\ &= \frac{1}{Re}\left(\frac{d}{dx}\hat{\mathrm{e}}_x+\frac{d}{dy}\hat{\mathrm{e}}_y\right)\cdot\left(\tilde{\mu_s}\phi_s\left(\frac{d\tilde{u_s}}{dy}\hat{\mathrm{e}}_x\hat{\mathrm{e}}_y+\frac{d\tilde{u_s}}{dy}\hat{\mathrm{e}}_y\hat{\mathrm{e}}_x\right)\right)\\ &= \frac{1}{Re}\frac{d}{dy}\cdot\left(\tilde{\mu_s}\phi_s\frac{d\tilde{u_s}(y)}{dy}\right)\hat{\mathrm{e}}_x\end{aligned}$$

We then have the final equations:

along x

$$\boxed{\frac{1}{Re}\ \frac{d}{dy}\ \left(\tilde{\mu_s}\phi_s\frac{d\tilde{u_s}(y)}{dy}\right)=-\delta(\tilde{u_f}-\tilde{u_s})-\tilde{\rho_s}\tilde{g}\phi_s}$$

along y

$$\boxed{\frac{1}{Re}\ \frac{d}{dy}\ \left(\tilde{\mu_n}\phi_s|\frac{d\tilde{u_s}(y)}{dy}|\right)=-\frac{d}{dy}\left(\gamma_s\left(\frac{d\phi_s}{dy}\right)^2\right)-\frac{d}{dy}(p_s\phi_s)}$$

**Compaction equation**

**Dimensional equation**

$$\frac{d\phi_s}{d_s t}=\frac{d\phi_s}{dt}+u_s\cdot\nabla\phi_s=Re_c\phi_s\phi_f(p_s-\beta_s-p_f+\nabla\cdot(\gamma_s\nabla\phi_s)) \tag{A.3}$$

**Non-dimensional equation**

$$\frac{d\phi_s}{d_s t}=\frac{d\phi_s}{d(\tilde{t}\cdot t_{ref})}+\tilde{u_s}u_{ref}\cdot\frac{1}{l_{ref}}\tilde{\nabla}\phi_s=Re_c\phi_s\phi_f\frac{1}{\rho_{ref}u_{ref}^2}\left(\tilde{p_s}-\tilde{\beta_s}-\tilde{p_f}+\tilde{\nabla}\cdot(\tilde{\gamma_s}\tilde{\nabla}\phi_s)\right) \tag{A.4}$$

$$\leftrightarrow\ \frac{u_{ref}}{l_{ref}}\frac{d\phi_s}{d\tilde{t}}+\tilde{u_s}u_{ref}\cdot\frac{1}{l_{ref}}\tilde{\nabla}\phi_s=\frac{\rho_{ref}u_{ref}l_{ref}}{\tilde{\mu_c}\mu_{ref}}\phi_s\phi_f\frac{1}{\rho_{ref}u_{ref}^2}\left(\tilde{p_s}-\tilde{\beta_s}-\tilde{p_f}+\tilde{\nabla}\cdot(\tilde{\gamma_s}\tilde{\nabla}\phi_s)\right)$$

$$\leftrightarrow\ \frac{d\phi_s}{d\tilde{t}}+\tilde{u_s}\cdot\tilde{\nabla}\phi_s=\frac{1}{\mu_c}\phi_s\phi_f\left(\tilde{p_s}-\tilde{\beta_s}-\tilde{p_f}+\tilde{\nabla}\cdot(\tilde{\gamma_s}\tilde{\nabla}\phi_s)\right)$$

**1D Stationnary Poiseuille flow**

The flow is stationnary;

$$\frac{d\phi_s}{d\tilde{t}} = 0$$

and unidirectionnal;

$$\tilde{u_s} \cdot \tilde{\nabla}\phi_s = \tilde{u_s}(y)\hat{\mathrm{e}}_x \cdot \frac{d\tilde{\phi_s}(y)}{dy}\hat{\mathrm{e}}_y = 0$$

The final equation is thus:

$$\boxed{\tilde{p_s} - \tilde{\beta_s} + \frac{d}{dy}\left(\tilde{\gamma_s}\frac{d}{dy}\phi_s\right) = 0}$$

# Bibliography


[1] Sofiane Benyahia, Madhava Syamlal, and Thomas J O'Brien. "Extension of Hill–Koch–Ladd drag correlation over all ranges of Reynolds number and solids volume fraction". In: *Powder Technology* 162.2 (2006), pp. 166–174.

[2] François Boyer, Olivier Pouliquen, and Élisabeth Guazzelli. "Dense suspensions in rotating-rod flows: normal stresses and particle migration". In: *Journal of Fluid Mechanics* 686 (2011), pp. 5–25.

[3] Sungyoung Choi et al. "Hydrophoretic sorting of micrometer and submicrometer particles using anisotropic microfluidic obstacles". In: *Analytical chemistry* 81.1 (2009), pp. 50–55.

[4] Dino Di Carlo et al. "Continuous inertial focusing, ordering, and separation of particles in microchannels". In: *Proceedings of the National Academy of Sciences* 104.48 (2007), pp. 18892–18897.

[5] Eugene C Eckstein, Douglas G Bailey, and Ascher H Shapiro. "Self-diffusion of particles in shear flow of a suspension". In: *Journal of Fluid Mechanics* 79.1 (1977), pp. 191–208.

[6] Sabri Ergun. "Fluid flow through packed columns". In: *Chem. Eng. Prog.* 48 (1952), pp. 89–94.

[7] Robin Fahraeus and Torsten Lindqvist. “The viscosity of the blood in narrow capillary tubes”. In: *American Journal of Physiology-Legacy Content* 96.3 (1931), pp. 562–568.

[8] C Gao, B Xu, and JF Gilchrist. “Mixing and segregation of microspheres in microchannel flows of mono-and bidispersed suspensions”. In: *Physical Review E* 79.3 (2009), p. 036311.

[9] AA Gavrilov and AV Shebelev. “Single-Fluid Model of a Mixture for Laminar Flows of Highly Concentrated Suspensions”. In: *Fluid Dynamics* 53.2 (2018), pp. 255–269.

[10] Somnath Ghosh et al. “Apparent wall-slip of colloidal hard-sphere suspensions in microchannel flow”. In: *Colloids and surfaces A: Physicochemical and engineering aspects* 491 (2016), pp. 50–56.

[11] Anne Gobin et al. “Fluid dynamic numerical simulation of a gas phase polymerization reactor”. In: *International journal for numerical methods in fluids* 43.10-11 (2003), pp. 1199–1220.

[12] *Granular.org Viscous stress*. `http://granular.org/viscous_stress.html`. Accessed: 2020-10-05.

[13] Elisabeth Guazzelli and Olivier Pouliquen. “Rheology of dense granular suspensions”. In: *Journal of Fluid Mechanics* 852 (2018).

[14] Da He and Ndy N Ekere. “Viscosity of concentrated noncolloidal bidisperse suspensions”. In: *Rheologica acta* 40.6 (2001), pp. 591–598.

[15] Dongeun Huh et al. “Gravity-driven microfluidic particle sorting device with hydrodynamic separation amplification”. In: *Analytical chemistry* 79.4 (2007), pp. 1369–1376.

[16] DM Husband et al. “Direct measurements of shear-induced particle migration in suspensions of bimodal spheres”. In: *Rheologica acta* 33.3 (1994), pp. 185–192.

[17] Marc S Ingber et al. “An improved constitutive model for concentrated suspensions accounting for shear-induced particle migration rate dependence on particle radius”. In: *International Journal of Multiphase Flow* 35.3 (2009), pp. 270–276.

[18] SC Jana, B Kapoor, and A Acrivos. “Apparent wall slip velocity coefficients in concentrated suspensions of noncolloidal particles”. In: *Journal of Rheology* 39.6 (1995), pp. 1123–1132.

[19] Dilhan M Kalyon. “Apparent slip and viscoplasticity of concentrated suspensions”. In: *Journal of Rheology* 49.3 (2005), pp. 621–640.

[20] 20A Karnis, HL Goldsmith, and SG Mason. “The kinetics of flowing dispersions: I. Concentrated suspensions of rigid particles”. In: *Journal of Colloid and Interface Science* 22.6 (1966), pp. 531–553.

[21] RM Klaver and CGPH Schroën. “A review of shear-induced particle migration for enhanced filtration and fractionation”. In: *Modeling Food Processing Operations*. Elsevier, 2015, pp. 211–233.

[22] Christopher J Koh, Philip Hookham, and L Gary Leal. “An experimental investigation of concentrated suspension flows in a rectangular channel”. In: *Journal of Fluid Mechanics* 266 (1994), pp. 1–32.

[23] Marko Korhonen et al. “Apparent wall slip in non-Brownian hard-sphere suspensions”. In: *The European Physical Journal E* 38.5 (2015), p. 46.

[24] Jason G Kralj et al. “Continuous dielectrophoretic size-based particle sorting”. In: *Analytical chemistry* 78.14 (2006), pp. 5019–5025.

[25] Irvin M Krieger and Thomas J Dougherty. “A mechanism for non-Newtonian flow in suspensions of rigid spheres”. In: *Transactions of the Society of Rheology* 3.1 (1959), pp. 137–152.

[26] Martin Kroupa, Miroslav Soos, and Juraj Kosek. “Slip on a particle surface as the possible origin of shear thinning in non-Brownian suspensions”. In: *Physical Chemistry Chemical Physics* 19.8 (2017), pp. 5979–5984.

[27] David Leighton and Andreas Acrivos. “The shear-induced migration of particles in concentrated suspensions”. In: *Journal of Fluid Mechanics* 181 (1987), pp. 415–439.

[28] Kevin Loutherback et al. “Improved performance of deterministic lateral displacement arrays with triangular posts”. In: *Microfluidics and nanofluidics* 9.6 (2010), pp. 1143–1149.

[29] A Ya Malkin and SA Patlazhan. “Wall slip for complex liquids–Phenomenon and its causes”. In: *Advances in colloid and interface science* 257 (2018), pp. 42–57.

[30] EWJ Mardles. “Viscosity of suspensions and the Einstein equation”. In: *Nature* 145.3686 (1940), pp. 970–970.

[31] Joseph M Martel and Mehmet Toner. “Inertial focusing in microfluidics”. In: *Annual review of biomedical engineering* 16 (2014), pp. 371–396.

[32] Stefan Miltenyi et al. “High gradient magnetic cell separation with MACS”. In: *Cytometry: The Journal of the International Society for Analytical Cytology* 11.2 (1990), pp. 231–238.

[33] Davide Monsorno, Christos Varsakelis, and MV Papalexandris. “A two-phase thermomechanical theory for granular suspensions”. In: *Journal of Fluid Mechanics* 808 (2016), pp. 410–440.

[34] Davide Monsorno, Christos Varsakelis, and MV Papalexandris. “Poiseuille flow of dense non-colloidal suspensions: The role of intergranular and nonlocal stresses in particle migration”. In: *Journal of Non-Newtonian Fluid Mechanics* 247 (2017), pp. 229–238.

[35] Jeffrey F Morris and Fabienne Boulay. “Curvilinear flows of noncolloidal suspensions: The role of normal stresses”. In: *Journal of rheology* 43.5 (1999), pp. 1213–1237.

[36] Prabhu R Nott and John F Brady. “Pressure-driven flow of suspensions: simulation and theory”. In: *Journal of Fluid Mechanics* 275 (1994), pp. 157–199.

[37] Sidhant Pednekar, Jaehun Chun, and Jeffrey F Morris. “Bidisperse and polydisperse suspension rheology at large solid fraction”. In: *Journal of Rheology* 62.2 (2018), pp. 513–526.

[38] Filip Petersson et al. “Free flow acoustophoresis: microfluidic-based mode of particle and cell separation”. In: *Analytical chemistry* 79.14 (2007), pp. 5117–5123.

[39] Ronald J Phillips et al. “A constitutive equation for concentrated suspensions that accounts for shear-induced particle migration”. In: *Physics of Fluids A: Fluid Dynamics* 4.1 (1992), pp. 30–40.

[40] G Segre and A Silberberg. “Radial particle displacements in Poiseuille flow of suspensions”. In: *Nature* 189.4760 (1961), pp. 209–210.

[41] Ryohei Seto and Giulio G Giusteri. “Normal stress differences in dense suspensions”. In: *Journal of Fluid Mechanics* 857 (2018), pp. 200–215.

[42] Kendra V Sharp. “Liquid flows in microchannels”. In: *The MEMS handbook* (2002), pp. 6–1.

[43] Olivier Simonin et al. “Drag force modelling in dilute to dense particle-laden flows with mono-disperse or binary mixture of solid particles”. In: 2016.

[44] Jonathan J Stickel and Robert L Powell. “Fluid mechanics and rheology of dense suspensions”. In: *Annu. Rev. Fluid Mech.* 37 (2005), pp. 129–149.

[45] Majid Ebrahimi Warkiani et al. “Membrane-less microfiltration using inertial microfluidics”. In: *Scientific reports* 5 (2015), p. 11018.

[46] CY Wen and YH Yu. “A generalized method for predicting the minimum fluidization velocity”. In: *AIChE Journal* 12.3 (1966), pp. 610–612.

[47] George M Whitesides. “The origins and the future of microfluidics”. In: *Nature* 442.7101 (2006), pp. 368–373.

[48] W Zhu. “Experimental study of dense suspension flow under cone-plate device”. In: *Ecole Centrale Marseille* (2016).

**UNIVERSITÉ CATHOLIQUE DE LOUVAIN**
**École polytechnique de Louvain**
Rue Archimède, 1 bte L6.11.01, 1348 Louvain-la-Neuve, Belgique | **www.uclouvain.be/epl**